Electronic Supplementary Material (ESI) for Energy & Environmental Science.

Supplementary information for "*The impact of binary water-CO2 isotherm models on the optimal performance of sorbent-based direct air capture processes.*"

John Young[a], Enrique García-Díez[a], Susana Garcia[a], Mijndert van der Spek[a]
[a]*Research Centre for Carbon Solutions, Heriot-Watt University, Edinburgh, EH14 4AS, United Kingdom*

SUPPLEMENTARY INFORMATION

SUMMARY OF AMINE-FUNCTIONALISED SORBENTS STUDIED FOR DAC

There is particular excitement around the use of amine-functionalised solid sorbents in DAC since they offer high affinity for CO_2 adsorption and very high selectivity to CO_2 over N_2.[1] The amines used are primary and secondary since functionalisation with tertiary amines has little effect on CO_2 capture.[2] There are various amines and solid supports used to synthesise such materials. Thus far, the most commonly used amine is polyethylenimine (PEI), which NASA has also utilised to reduce CO_2 concentrations on spacecraft.[3–8] However, there are diffusional limitations of using PEI due to its large molecular size.[9] Other amines previously studied include ethylenediamine (en), N, N'-dimethylethylenediamine (mmen), and tetraethylpentamine (TEPA).[10–12]. Silica is by far the most studied solid support so far, although it may not be the most suitable due to higher costs and potential instability under steam purging conditions.[8,13–19] Currently, the adsorbent produced with the highest CO_2 capacity under DAC conditions (400 ppm CO2 in air) is a TEPA functionalised silica sorbent (SBA-15) with a capacity of 3.59 mmol g^{-1}.[12,20] However, it is important to stress that capacity is one small metric and does not per se ensure good process performance of a material.[21] Nevertheless, various other solid supports have been investigated in the context of DAC, such as metal-organic frameworks (MOFs), alumina, carbon black, cellulose, and resins.[10,11,22–25] A summary of some materials studied for DAC to date is available in, Table S1.

*Table S1 A selection of solid sorbents that have been investigated for DAC along with the data supplied by the authors. *Value only provided in cm^3 cm^{-3} for CO_2 uptake of SGU-29. The value is between the quoted values of Mg-MOF-74 and SIFSIX-3-Cu*

Material	**Class of materials**	**Sorption principle**	**Equilibrium capacity under dry DAC adsorption conditions / mmol g^{-1}**	**CO2 heat of adsorption / kJ mol^{-1}**	**Cycling stability data**	**Reference**
PEI-γ-Alumina	Alumina	Chemisorption	1.95	Unavailable	Available	[6,22]
CB-g-xPCMS-OH$^-$	Carbon black	Chemisorption	0.14	Unavailable	Unavailable	[23]
CB-g-p(NMe^{3+}-MSOH$^-$)	Carbon black	Chemisorption	0.14	Unavailable	Unavailable	[23]
APDES-NFC-FD	Cellulose	Chemisorption	1.11	50	Available	[24,26–29]
En-Mg$_2$(dobpdc)	MOF	Chemisorption	2.83	50	Available	[10]
mmen-Mg$_2$(dobpdc)	MOF	Chemisorption	2.00	73	Available	[11,21]
Mg-MOF-74-EN	MOF	Chemisorption	1.51	Unavailable	Available	[30]
Zn-aminotriazolato-oxalate	MOF	Chemisorption	1.60	38.6	Unavailable	[31]
MIL-101(Cr)-TREN	MOF	Chemisorption	2.80	Unavailable	Available	[32]
MIL-101(Cr)-PEI-800	MOF	Chemisorption	1.06	55	Available	[32,33]
Cr-MIL-101-SO$_3$H-TAEA	MOF	Chemisorption	1.12	Unavailable	Available	[34]
HP20/PEI-50	Resin	Chemisorption	2.26	Unavailable	Available	[4]
RFAS	Resin	Chemisorption	1.71	Unavailable	Available	[35]
Lewatit® VP OC 1065	Resin	Chemisorption	1.10	70-80	Unavailable	[36–39]
PPN-6-CH$_2$DETA	Resin	Chemisorption	1.04	53.8	Unavailable	[40]
PPN-6-CH$_2$Cl	Resin	Chemisorption	0.00	20	Unavailable	[40]
PPN-6-CH$_2$EDA	Resin	Chemisorption	0.15	60	Unavailable	[40]
I-200	Resin	Chemisorption	0.74	Unavailable	Unavailable	[41–43]
HIPE	Resin	Chemisorption	0.72	Unavailable	Available	[44]
HIPE templated p(NMe^{3+}-MSOH$^-$)	Resin	Chemisorption	0.49	Unavailable	Unavailable	[45]
Colloidial crystal templated p(NMe^{3+}-MSOH$^-$)	Resin	Chemisorption	0.37	Unavailable	Unavailable	[45]

TEPA-SBA-15	Silica	Chemisorption	3.59	Unavailable	Available	[12,20]
PEI-CA-SiO$_2$ fiber	Silica	Chemisorption	0.61	Unavailable	Available	[8]
HMS-10a-PEI (50)	Silica	Chemisorption	2.40	Unavailable	Available	[13]
PEI-Silica	Silica	Chemisorption	2.36	Unavailable	Available	[46]
FS-PEI	Silica	Chemisorption	2.34	83	Available	[15]
A-PEI-Silica	Silica	Chemisorption	2.26	Unavailable	Available	[46]
T-PEI-Silica	Silica	Chemisorption	2.19	Unavailable	Available	[46]
HMS-12a-PEI (50)	Silica	Chemisorption	2.15	Unavailable	Available	[13]
PEIBr_MCF	Silica	Chemisorption	1.74	Unavailable	Available	[47]
Hyperbranched aminosilica (HAS)	Silica	Chemisorption	1.72	Unavailable	Available	[16]
FS-PEI	Silica	Chemisorption	1.70	82-87	Unavailable	[14]
TRI-PE-MCM-41	Silica	Chemisorption	1.19	92	Unavailable	[17]
PEILn_MCF	Silica	Chemisorption	1.05	Unavailable	Unavailable	[47]
PAA_MCF	Silica	Chemisorption	0.86	Unavailable	Available	[47]
PEI/Zr-SBA-15	Silica	Chemisorption	0.85	Unavailable	Available	[48]
SBA-15-PEG-PEI	Silica	Chemisorption	0.79	Unavailable	Unavailable	[18]
Poly(l-lysine) brush–mesoporous silica hybrids	Silica	Chemisorption	0.60	Unavailable	Available	[19]
SBA-15-CTAB-PEI	Silica	Chemisorption	0.55	Unavailable	Unavailable	[18]
MCF-APS	Silica	Chemisorption	0.54	130	Unavailable	[2]
SI-AEATPMS	Silica	Chemisorption	0.44	Unavailable	Available	[49]
MCF-MAPS	Silica	Chemisorption	0.17	88	Unavailable	[2]
APTES-SBA-15	Silica	Chemisorption	0.14	65	Unavailable	[50]
SGU-29	Copper silicate	Physisorption	(25cm^3 cm^{-3})*	51.3	Available	[51]
SIFSIX-3-Cu	MOF	Physisorption	1.24/0.32	54	Limited	[52,53]
UiO-66-NH$_2$	MOF	Physisorption	0.25	35.1	Unavailable	[53]
SIFSIX-3-Ni	MOF	Physisorption	0.18	Unavailable	Available	[20]
Mg-MOF-74	MOF	Physisorption	0.088/0.14	47	Available	[20,52]
SIFSIX-3-Zn	MOF	Physisorption	0.13	45	Unavailable	[52]
Ni-4-PyC	MOF	Physisorption	0.07	Unavailable	Unavailable	[53]

MOOFOUR-1-Ni	MOF	Physisorption	0.06	Unavailable	Unavailable	[53]
ZIF-8	MOF	Physisorption	0.05	Unavailable	Unavailable	[53]
HKUST-1	MOF	Physisorption	0.05	Unavailable	Available	[20]
DMOF-1	MOF	Physisorption	0.04	Unavailable	Unavailable	[53]
DICRO-3-Ni-i	MOF	Physisorption	0.04	Unavailable	Unavailable	[53]
UiO-66	MOF	Physisorption	0.02	Unavailable	Unavailable	[53]
NbOFFIVE-1-Ni	MOF	Physisorption	1.30	55	Unavailable	[54]
Li-LSX	Zeolite	Physisorption	1.34	51	Unavailable	[50]
Na-LSX	Zeolite	Physisorption	0.87	45	Unavailable	[50]
Ca-LSX	Zeolite	Physisorption	0.76	39	Unavailable	[50]
K-LSX	Zeolite	Physisorption	0.67	43	Unavailable	[50]
NaX	Zeolite	Physisorption	0.41	40	Unavailable	[50]
CaY	Zeolite	Physisorption	0.14	46	Unavailable	[50]
NaY	Zeolite	Physisorption	0.08	30	Unavailable	[50]
Zeolite 13X	Zeolite	Physisorption	0.03	31.86	Available	[20,55]

DVS VACUUM – FURTHER INFORMATION ON EXPERIMENTAL METHODS

We have, previously, described the DVS Vacuum and its methods in detail.[56] The following section is an adapted excerpt from this work.

In the experiments presented in this work, the gas and vapour used are CO2 and water. A turbomolecular pump enables the pressure in the chamber to reach as low as 10^{-6} mbar. This ensures very thorough outgassing of the sample prior to adsorption. The vacuum pump, coupled with various control valves, allows very accurate control of the sorption chamber pressure during adsorption and desorption measurements. The temperature in the sorption chamber can range from room temperature up to 400°C whilst the whole system, apart from the gas storage and vacuum pumps, is inside an incubator (temperature-controlled enclosure) operating in the temperature range from 20 up to 70°C. The incubator temperature sets the maximum limit of the solvent's (here, water) partial pressure in the sorption chamber as the saturation pressure at this temperature. The set partial pressure of water is introduced under vacuum without the interference of a carrier gas at the set experimental temperature. The sample's weight is measured directly and continuously using Surface Measurement Systems' UltraBalance with a resolution of 0.1 µg. The sorption measurements can be done in a fixed time mode or mass equilibrium mode where the mass equilibrium criterion is set as the change in mass per minute (dm/dt). The control software automatically calculates and checks the dm/dt criterion against the set dm/dt value. When the sample's mass has reached equilibrium at a certain partial pressure of the gas or vapour, the control software automatically moves on to the next partial pressure step in the method. In this study mass equilibrium mode is used.

The DVS Vacuum can be operated in a "dynamic", "semi-static", or "static" mode. In dynamic mode, the downstream and upstream sorbate flow is controlled, while changes in sample mass are continuously monitored. In a typical experiment, vapour or gas flows at a constant rate over a sample while the total system pressure is kept constant. Meanwhile, in static mode, the upstream and downstream control valves are closed upon the injection of a sorbate in the chamber (similar to manometric systems). At the same time, changes in sample mass are continuously monitored using the UltraBalance. There are two options for static mode: semi-static and true static. The difference between these two options is that in semi-static mode, more sorbate molecules are added to the chamber when the pressure inside the vacuum chamber decreases below the set pressure due to sorption of molecules by the sample. On the other hand, in true static mode, when the partial pressure drops below the set pressure, more molecules are not injected into the chamber and the sample is simply left to equilibrate.

CO_2 experimental method

Table S2 Typical CO_2 adsorption experiment conditions.

Step	Pressure set point [bar]	Temperature set point [℃]	Gas/vapour	Mode
1	0	100	None	Semi-static
2	0	$T_{experiment}$	None	Semi-static
3	0.0002	$T_{experiment}$	CO_2	Semi-static
4	0.0004	$T_{experiment}$	CO_2	Semi-static
5	0.0006	$T_{experiment}$	CO_2	Semi-static
6	0.001	$T_{experiment}$	CO_2	Semi-static
7	0.01	$T_{experiment}$	CO_2	Semi-static
8	0.1	$T_{experiment}$	CO_2	Semi-static
9	0.2	$T_{experiment}$	CO_2	Semi-static
10	0.3	$T_{experiment}$	CO_2	Semi-static
11	0.4	$T_{experiment}$	CO_2	Semi-static
12	0.5	$T_{experiment}$	CO_2	Semi-static
13	0.6	$T_{experiment}$	CO_2	Semi-static
14	0.7	$T_{experiment}$	CO_2	Semi-static
15	0.8	$T_{experiment}$	CO_2	Semi-static
16	0.9	$T_{experiment}$	CO_2	Semi-static
17	1.01325	$T_{experiment}$	CO_2	Semi-static
18	0.9	$T_{experiment}$	CO_2	Semi-static
19	0.8	$T_{experiment}$	CO_2	Semi-static
20	0.7	$T_{experiment}$	CO_2	Semi-static
21	0.6	$T_{experiment}$	CO_2	Semi-static
22	0.5	$T_{experiment}$	CO_2	Semi-static
23	0.4	$T_{experiment}$	CO_2	Semi-static
24	0.3	$T_{experiment}$	CO_2	Semi-static
25	0.2	$T_{experiment}$	CO_2	Semi-static
26	0.1	$T_{experiment}$	CO_2	Semi-static
27	0.01	$T_{experiment}$	CO_2	Semi-static
28	0.001	$T_{experiment}$	CO_2	Semi-static
29	0.0006	$T_{experiment}$	CO_2	Semi-static
30	0.0004	$T_{experiment}$	CO_2	Semi-static

31	0.0002	$T_{experiment}$	CO_2	Semi-static
32	0	$T_{experiment}$	CO_2	Semi-static

H_2O experimental method

Table S3 Typical H_2O adsorption experiment conditions. For each step the flow rate of water was set according to the flow rate recommended by the DVS Vacuum manual for that specific absolute pressure.

Step	**Relative humidity [%]**	**Temperature set point [℃]**	**Gas/vapour**	**Mode**
1	0	100	None	Dynamic
2	0	$T_{experiment}$	None	Dynamic
3	2.5	$T_{experiment}$	H_2O	Dynamic
4	5	$T_{experiment}$	H_2O	Dynamic
5	7.5	$T_{experiment}$	H_2O	Dynamic
6	10	$T_{experiment}$	H_2O	Dynamic
7	15	$T_{experiment}$	H_2O	Dynamic
8	20	$T_{experiment}$	H_2O	Dynamic
9	25	$T_{experiment}$	H_2O	Dynamic
10	30	$T_{experiment}$	H_2O	Dynamic
11	35	$T_{experiment}$	H_2O	Dynamic
12	40	$T_{experiment}$	H_2O	Dynamic
13	50	$T_{experiment}$	H_2O	Dynamic
14	60	$T_{experiment}$	H_2O	Dynamic
15	70	$T_{experiment}$	H_2O	Dynamic
16	80	$T_{experiment}$	H_2O	Dynamic
17	90	$T_{experiment}$	H_2O	Dynamic
18	80	$T_{experiment}$	H_2O	Dynamic
19	70	$T_{experiment}$	H_2O	Dynamic
20	60	$T_{experiment}$	H_2O	Dynamic
21	50	$T_{experiment}$	H_2O	Dynamic
22	40	$T_{experiment}$	H_2O	Dynamic
23	35	$T_{experiment}$	H_2O	Dynamic
24	30	$T_{experiment}$	H_2O	Dynamic
25	25	$T_{experiment}$	H_2O	Dynamic
26	20	$T_{experiment}$	H_2O	Dynamic
27	15	$T_{experiment}$	H_2O	Dynamic
28	10	$T_{experiment}$	H_2O	Dynamic
29	7.5	$T_{experiment}$	H_2O	Dynamic

30	5	$T_{experiment}$	H_2O	Dynamic
31	2.5	$T_{experiment}$	H_2O	Dynamic
32	0	$T_{experiment}$	H_2O	Dynamic

Co-adsorption experimental method

Table S4 Typical co-adsorption experiment conditions. Here, P_{RH}*, is the partial pressure of water corresponding to relative humidity and temperature desired.*

Step	**Pressure set point [bar]**	**Temperature set point [℃]**	**Gas/vapour**	**Mode**
1	0	100	None	Semi-static
2	0	$T_{experiment}$	None	Semi-static
3	P_{RH}	$T_{experiment}$	H_2O	Semi-static
4	P_{RH} + 0.0002	$T_{experiment}$	CO_2	Semi-static
5	P_{RH} + 0.0006	$T_{experiment}$	CO_2	Semi-static
6	P_{RH} + 0.01	$T_{experiment}$	CO_2	Semi-static
7	P_{RH} + 0.1	$T_{experiment}$	CO_2	Semi-static
8	P_{RH} + 0.2	$T_{experiment}$	CO_2	Semi-static
9	P_{RH} + 0.6	$T_{experiment}$	CO_2	Semi-static
10	1.01325	$T_{experiment}$	CO_2	Semi-static

DVS VACUUM DATA

Examples of raw gravimetric data

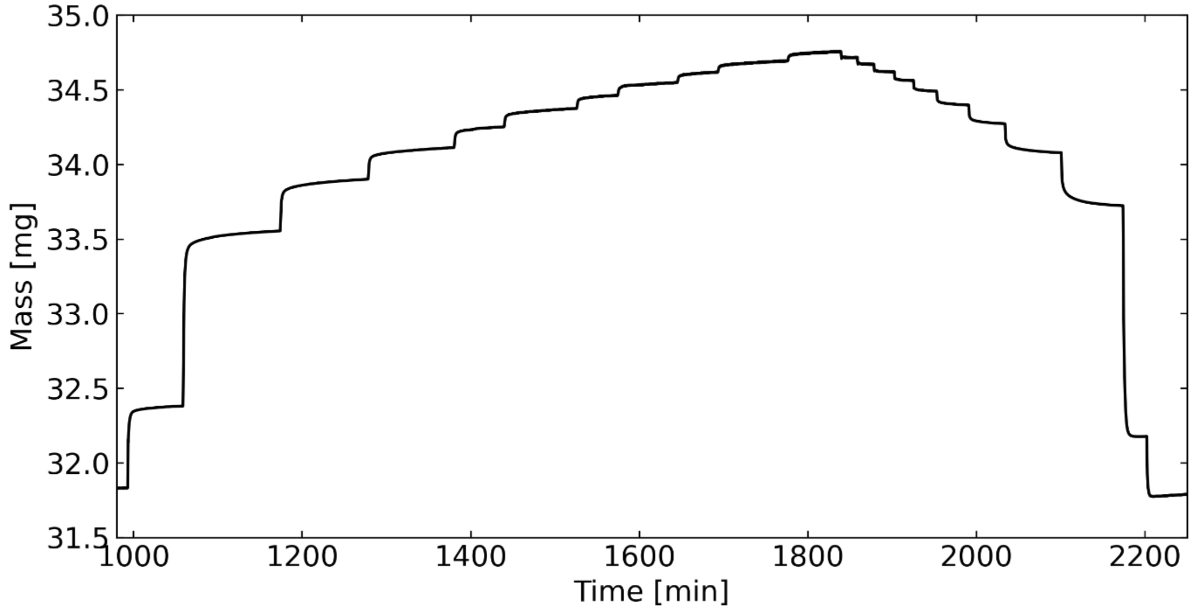

Figure S1 A graph showing mass change over time for a CO_2 *isotherm experiment at 75°C.*

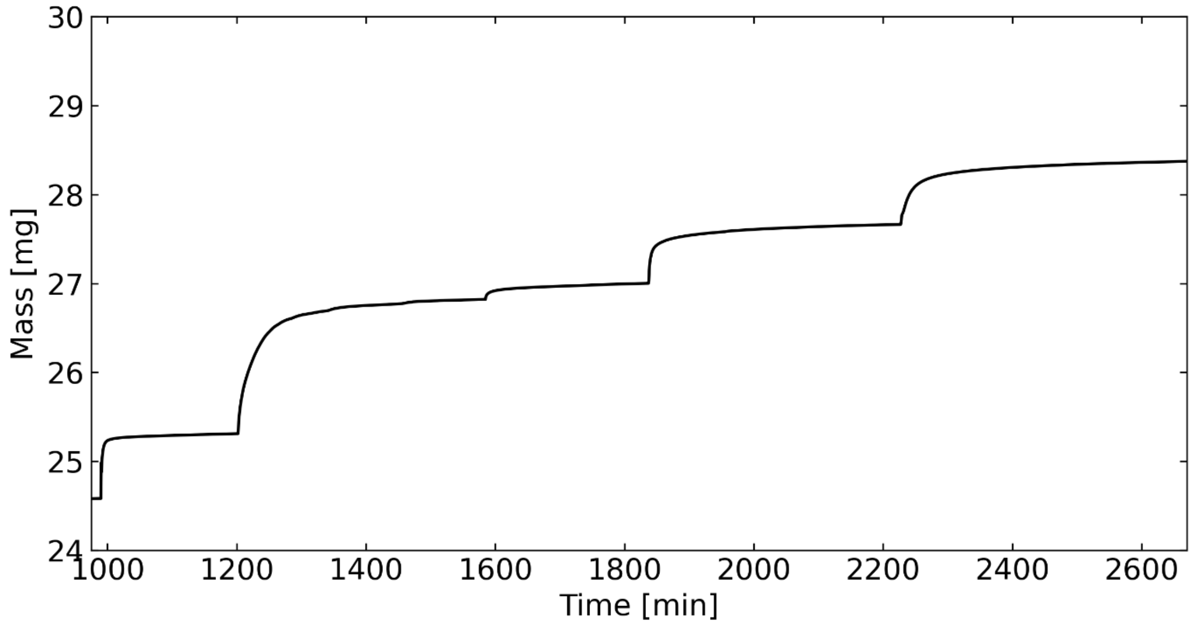

Figure S2 An example of mass change over time for a co-adsorption H_2O-CO_2 isotherm experiment at 25°C and 30% RH. The first mass change step we can see is a water adsorption step, with the subsequent ones being CO_2 adsorption.

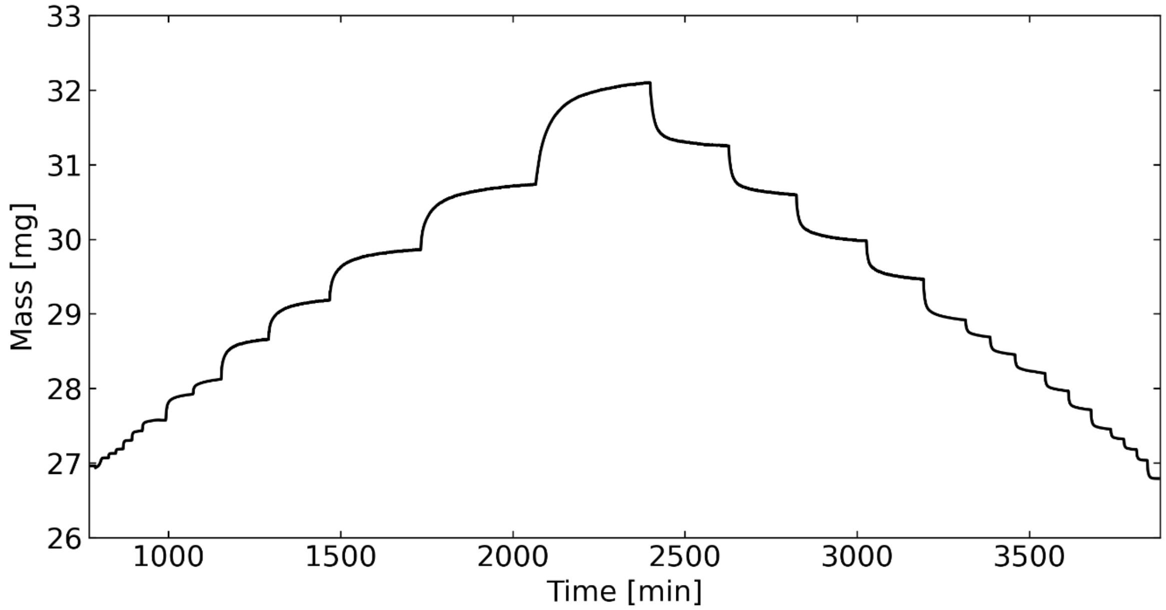

Figure S3 A graph showing mass change over time for a H_2O isotherm experiment at 25°C.

A note on the initial and final masses in Figures S1 and S3

The mass of the sample ends slightly lower than it starts in Figures S1 and S3. After discussions with the manufacturer of the DVS Vacuum, it was clarified that there could not be mass lost from the sample pan. The only explanation left is that there is a slight drift in the balance that is exaggerated over the very long experimental times. The mass difference accounts for around 3% of the maximum loading in both cases. We want to note that this would affect the desorption branches more than the adsorption branches and lead to a slightly higher desorption branch than those depicted in Figures S6 and S10, and an even more visible hysteresis. The adsorption branches are also more critical in this study as they are fitted to isotherm models for process modelling.

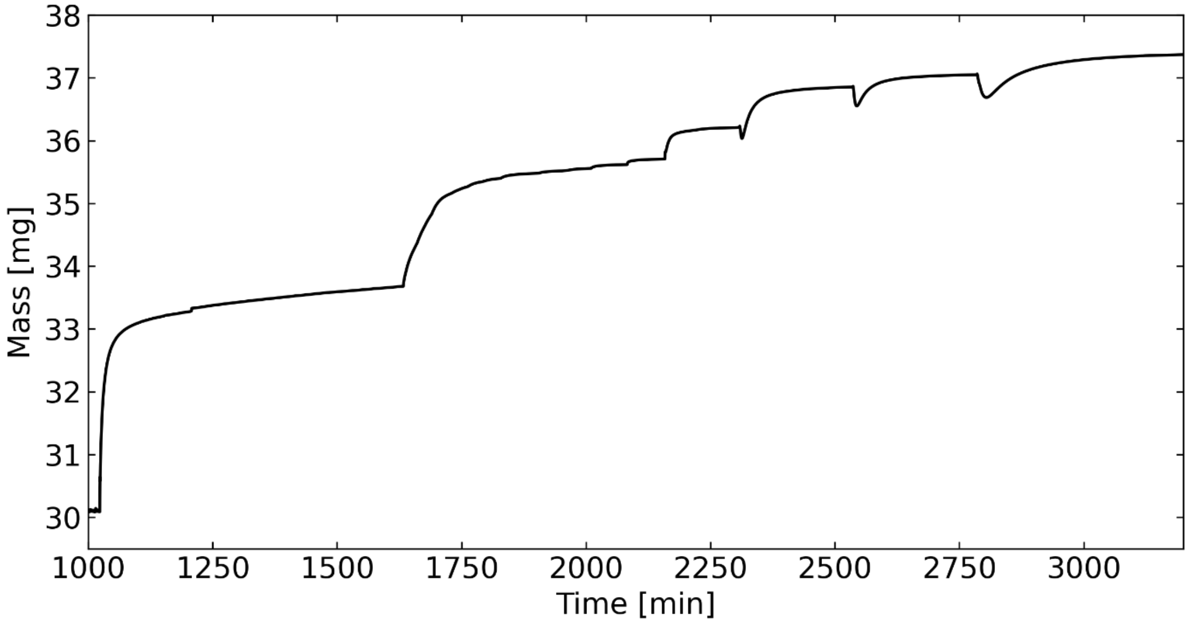

Figure S4 An example of mass change over time for a co-adsorption H_2O*-*CO_2 *isotherm experiment at 25°C and 80% RH. The first mass change step we can see is a water adsorption step, with the subsequent ones being* CO_2 *adsorption. The sharp decrease in mass in the later* CO_2 *steps suggests that* H_2O *may be desorbing, so the assumption that* CO_2 *does not affect* H_2O *adsorption may no longer hold at these higher relative humidities.*

PURE N_2 ISOTHERMS

Meanwhile, N_2 isotherms were measured using a volumetric method with the Micromeritics' Gemini VII.[57] The quantity of N_2 adsorbed was very low, and this method eliminated any mismeasurements due to flow effects or impurities. During these measurements, the sample's temperature was kept constant through submergence in a liquid nitrogen bath or an ice bath for two of the experiments. For the highest temperature (20 °C) experiment, the adsorption was performed at room temperature with no temperature control. However, the room temperature was monitored throughout and observed to only vary between 19 and 21°C. The resultant isotherms are shown in Figure S5.

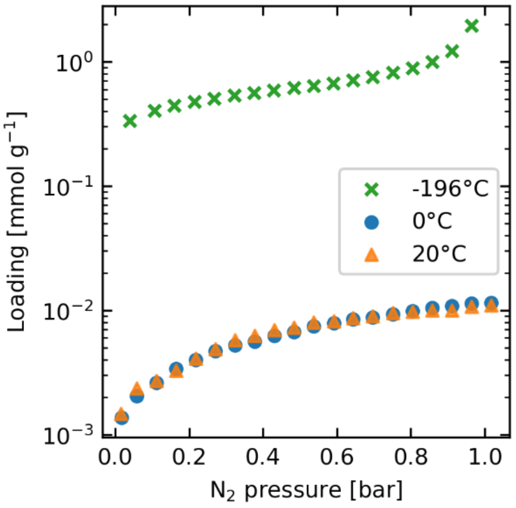

Figure S5 Nitrogen isotherms at 3 different temperatures. Note that the loading axis is logarithmic.

PURE CO_2 ISOTHERMS

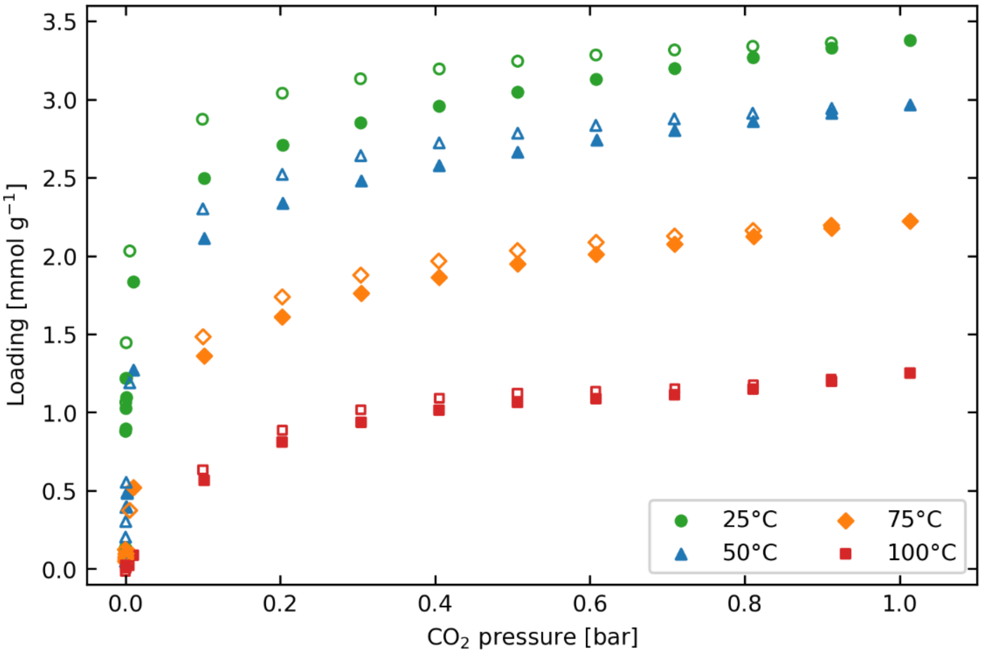

Figure S6 Pure CO_2 isotherms. The adsorption branch is shown by the solid markers whilst the desorption branch is shown by the empty markers.

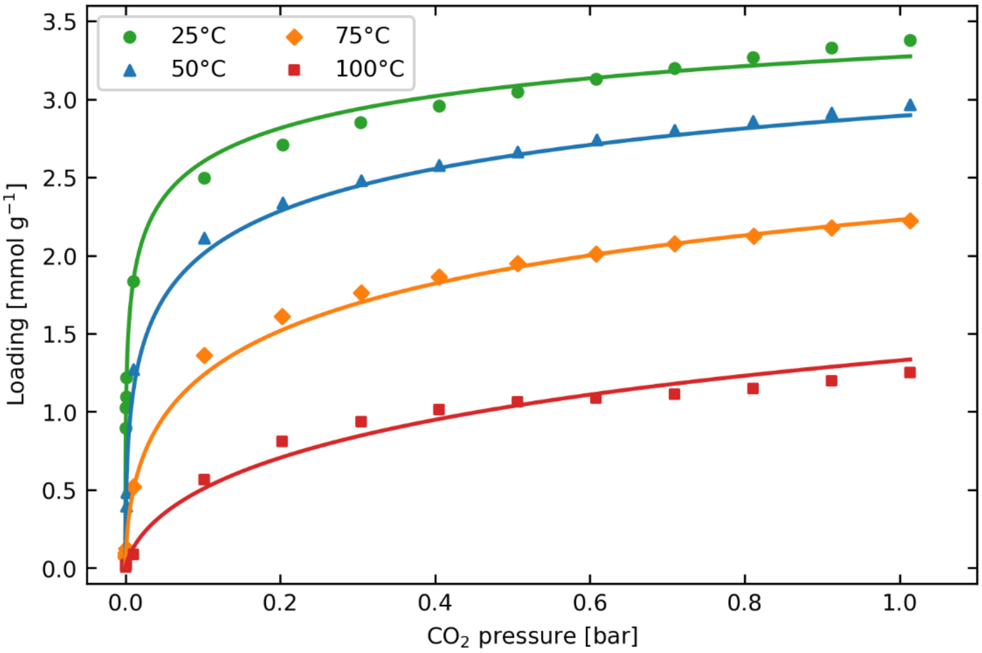

Figure S7 Pure CO_2 isotherms with the modelling fit. The experimental data is shown by the solid and the Toth model fit to the adsorption branches is shown by the lines.

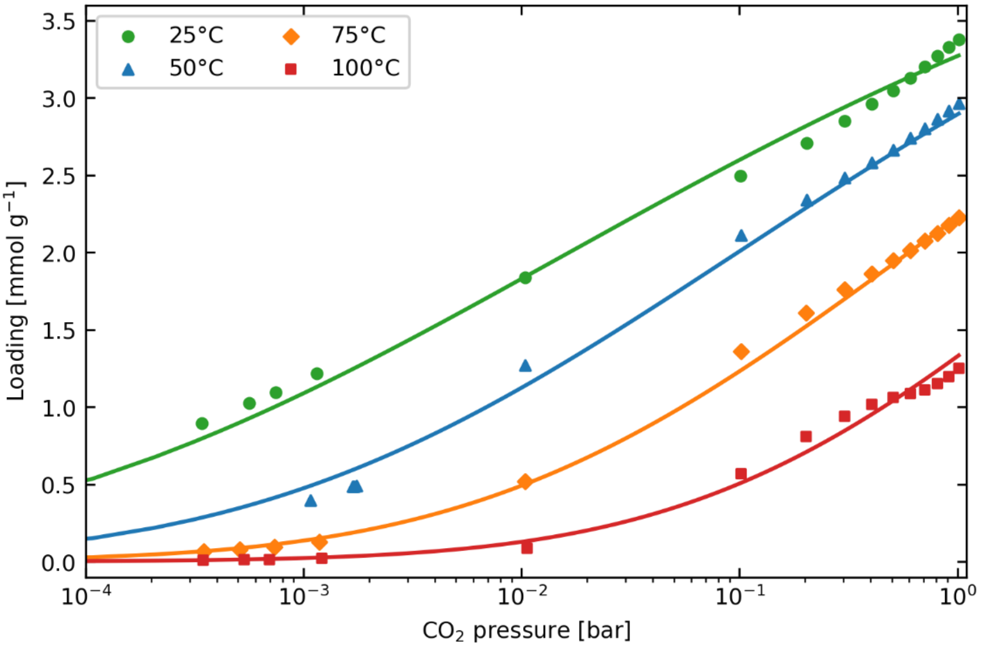

Figure S8 Pure CO_2 isotherms with the modelling fit. Data presented on a log scale on the x-axis. The experimental data is shown by the solid and the Toth model fit to the adsorption branches is shown by the lines.

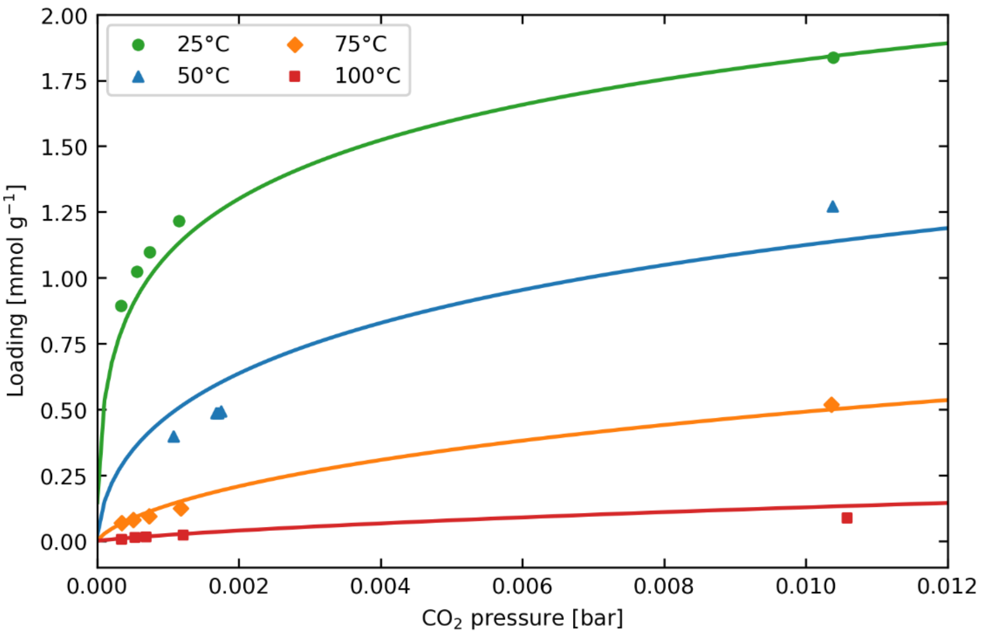

Figure S9 Pure CO2 isotherms with the modelling fit, zoomed up on the low-pressure region. The experimental data is shown by the solid and the Toth model fit to the adsorption branches is shown by the lines.

Figure S9 shows the low-pressure regions of the CO_2 isotherms including the modelling fit. Equal weight was given to all points in the fitting, and since there is a higher density of experimental points in the low-pressure region this gave a greater weight to this region. An agreeable fit is found in this region, which of course is especially important for DAC modelling due to the low partial pressure of CO_2 in air.

PURE H_2O ISOTHERMS

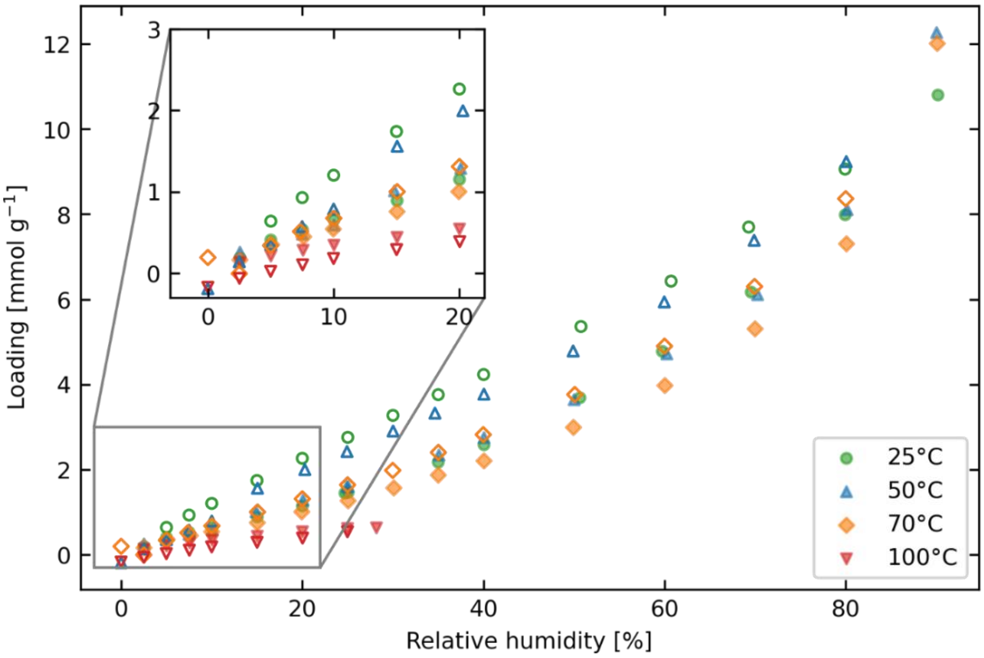

Figure S10 Pure H_2O isotherms. The adsorption branch is shown by the solid markers whilst the desorption branch is shown by the empty markers. Note the significant hysteresis, tested not to be an artefact of incomplete equilibrium.

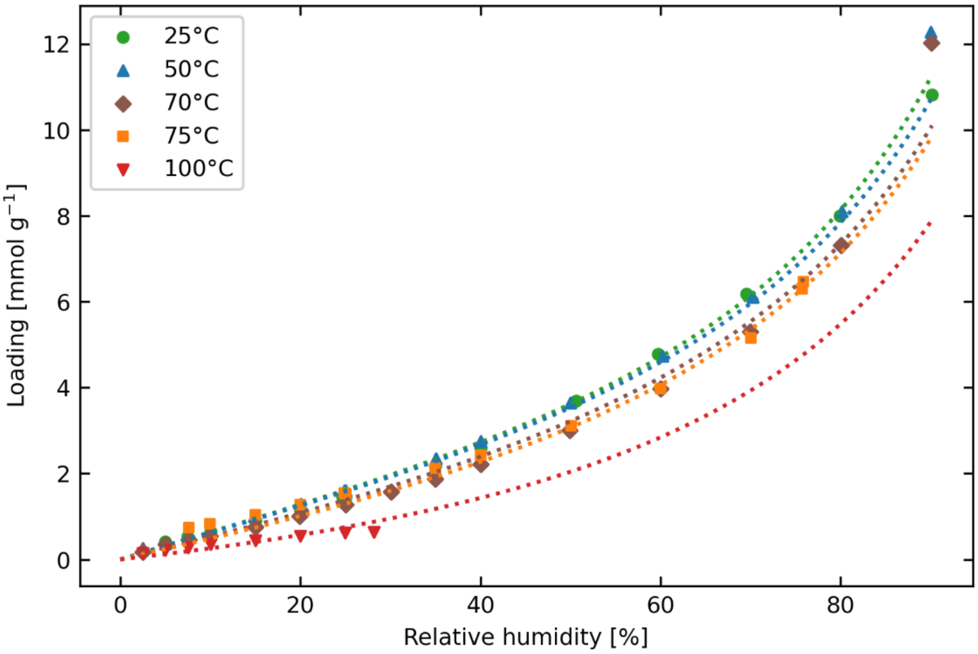

Figure S11 Pure H_2O isotherms with the modelling fit. The experimental data is shown by the markers and the GAB model fit to the adsorption branches is shown by the lines. The points at 90% relative humidity were not used for fitting since the loading did not follow the expected trend with temperature. This is potentially due to any experimental error exaggerated by the unlimited multilayer growth at high humidities and the very long times required to reach equilibrium.

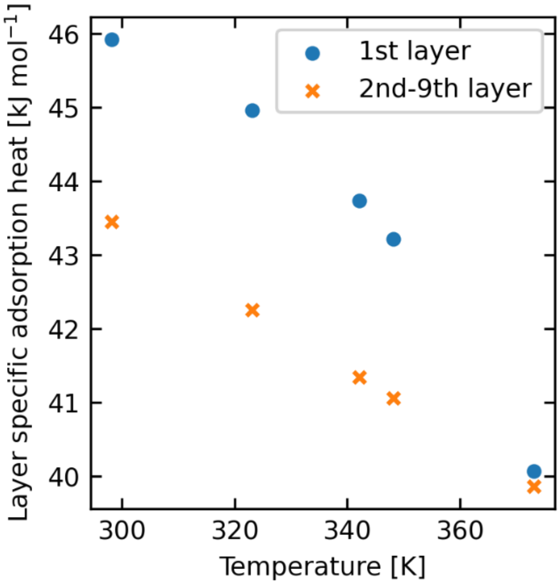

Figure S12 Magnitude of adsorption heats specific to layers, as defined by the GAB model, plotted against temperature.

CO-ADSORPTION ISOTHERMS

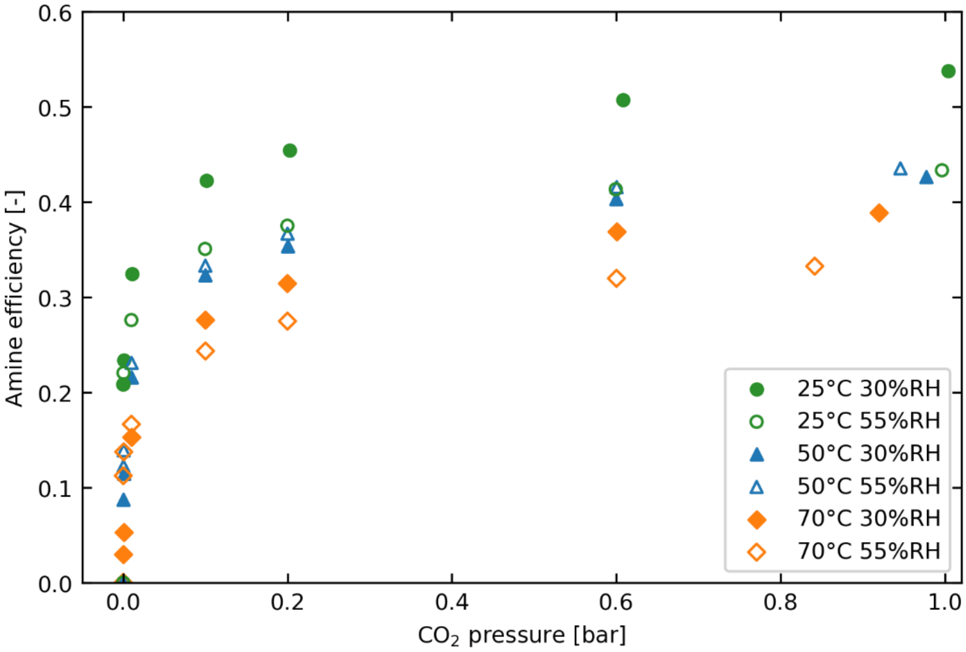

Figure S13 Showing the co-adsorption isotherms in the form of amine efficiency using the amine loading of 6.7 mmol g^{-1} reported by Alesi and Kitchin.[59]

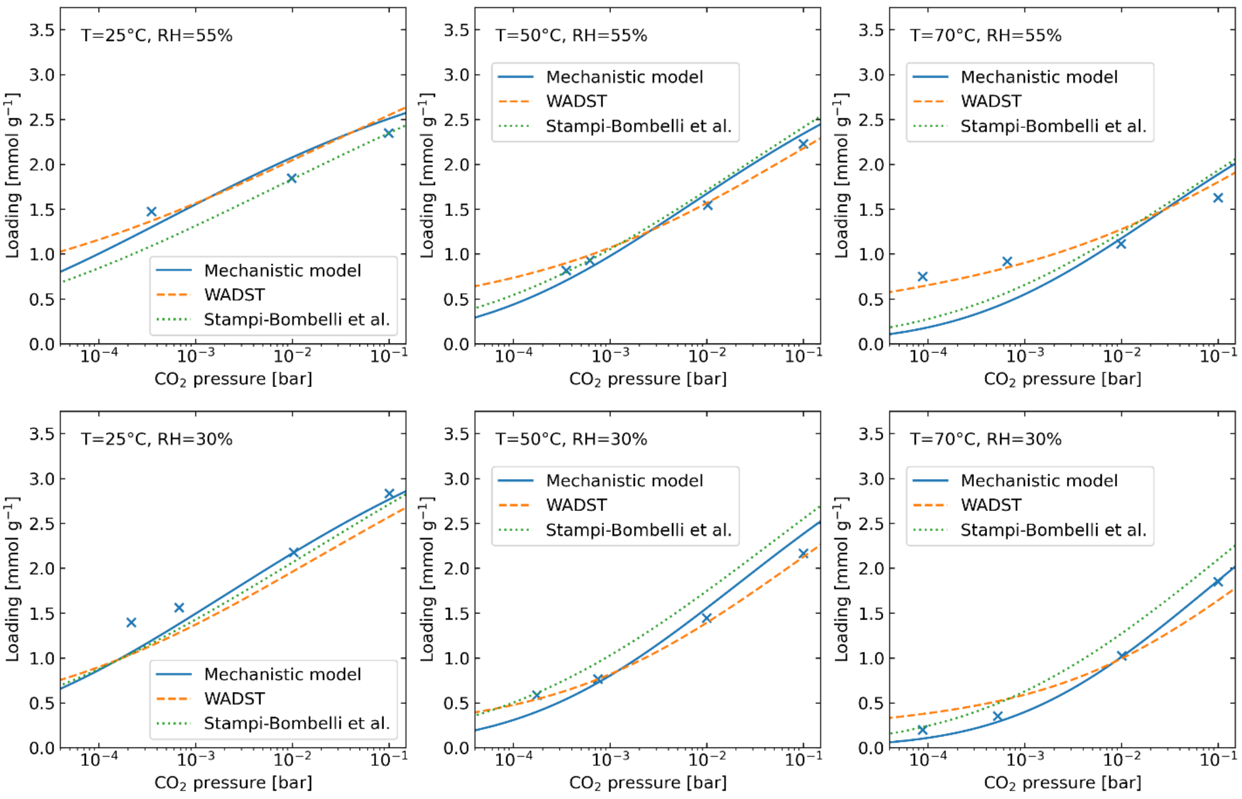

Figure S14 Experimental co-adsorption CO2 isotherms (markers), at various temperatures (T) and relative humidities (RH), fitted to an empirical literature co-adsorption model from Stampi-Bombelli et al. and the two models presented in this work. This figure shows the low-pressure range on a log scale.

COLUMN MODELLING

Pressure drop

The pressure drop equation for a packed bed, studied by Ergun is:[58]

$$\frac{\partial P}{\partial z} = -\frac{150\mu v(1-\epsilon_b)^2}{2R_p\epsilon_b^3} - \frac{1.75\rho_f v|v|(1-\epsilon_b)}{2R_p\epsilon_b^3}$$

Where μ [Pa s] is the viscosity of the fluid, R_p [m] is pellet radius, and ρ_f [kg m^{-3}] is the fluid density.

Isotherm and kinetics

Kinetic equations are used to describe the rate of adsorption. In these equations, one factor contributing to the driving force for adsorption is saturation loading, which is represented by temperature-dependent isotherms. These isotherms are described in the modelling and results sections. The linear driving force (LDF) model is a simple approach to lumping kinetic resistances and is shown in below: [60]

$$\frac{\partial q_i}{\partial t} = k_{LDF,i}(q_{sat,i} - q_i)$$

Where $k_{LDF,i}$ is the LDF rate constant for component i, and $q_{sat,i}$ [mol kg^{-1}] is the saturation loading for component i calculated from the isotherms.

Constitutive equations

An equation of state was required to relate concentration to pressure and temperature. For DAC, where the pressures and temperatures are low to ambient, the ideal gas equation is sufficient. This is shown below:

$$c_i = \frac{y_i P}{RT}$$

Where y_i [-] is the gas phase mole fraction of component i.

The saturation pressure of water allows the calculation of relative humidity and is related to temperature. One of the more accurate correlations describing this relation is the Arden Buck equation shown below: [61]

$$P_{sat} = 611.21 \exp\left(\left(18.678 - \frac{T - 273.15}{234.5}\right)\frac{T - 273.15}{T - 16.01}\right)$$

Where P_{sat} [Pa] is the saturation pressure. The following equation from Ruthven[62] can be used to calculate the axial mass dispersion:

$$D_L = \gamma_1 D_m + \frac{\gamma_2 d_p u}{\epsilon_b}$$

γ_1 [-] is 0.7 whilst γ_2 [-] is 0.5. D_m [m^2 s^{-1}] is the molecular diffusivity of the mixture, and d_p is particle diameter. The velocity u [m s^{-1}] will be fixed as the feed velocity, v_{feed} [-], for adsorption and pressurisation steps, and 0 for all other steps. The thermal dispersion can be calculated from the likeness condition:

$$\lambda_L = D_L C_{p,f} \frac{P}{RT}$$

Boundary and initial conditions

Boundary and initial conditions were defined to solve the set of equations. The boundary conditions in the model for each step in a TVSA cycle are detailed in Table S5. For the breakthrough modelling, used to fit the mass transfer coefficients, the adsorption step boundary conditions were applied throughout. The subscript *feed* applies to the feed conditions, whilst *out* applies to the column exit. Two new variables are introduced here, $\alpha_{blowdown}$ [-] and $\alpha_{pressurisation}$ [-] and they are used to describe the exponential relationship between pressure and time caused by valve resistances upstream and downstream of the column. Streb et al. previously found that a reasonable value of $\alpha_{blowdown}$ was 0.11.[63] The same value is also used for $\alpha_{pressurisation}$. In reality this value may be higher, but the effect on the modelling results is expected to small, and it is unlikely that the operator would want to pressurise the column too quickly, so they may enforce a slower rate of pressurisation. In any case, the vacuum and pressurisation times are very small compared to the time of the whole cycle, and these valve resistance parameters do not noticeably affect the model solution for this DAC case.

The initial conditions are shown below:.

$$q_i = q_{i,initial}$$

$$y_i = y_{i,initial}$$

$$\mathrm{T} = T_{initial}$$

$$\mathrm{P} = P_{initial}$$

Where $q_{i,initial}$ is the initial loading of component i, $y_{i,initial}$ is the initial mole fraction of component i in the gas phase, $T_{initial}$ is the initial temperature, and $P_{initial}$ is the initial pressure.

Table S5 Boundary conditions for each step in a TVSA cycle that exists in the model.

Step	Column position	Equation
Adsorption	$z = 0$	$v_{feed} c_{i,feed} = v c_i - D_L \epsilon_b \frac{\partial c_i}{\partial z}$
		$\Sigma_i v_{feed} c_{i,feed} = cv$
		$T_{feed} C_{p,f,feed} v_{feed} \Sigma_i c_{i,feed} = T C_{p,f} v \Sigma_i c_i - \lambda_L \epsilon_b \frac{\partial T}{\partial z}$
	$z = L$	$P = P_{out}$
Pressurisation	$z = 0$	$v_{feed} c_{i,feed} = v c_i - D_L \epsilon_b \frac{\partial c_i}{\partial z}$
		$\frac{\partial P}{\partial z} = \alpha_{pressurisation}(P_{feed} - P)$
		$T_{feed} C_{p,f,feed} v_{feed} \Sigma_i c_{i,feed} = T C_{p,f} v \Sigma_i c_i - \lambda_L \epsilon_b \frac{\partial T}{\partial z}$
	$z = L$	$v = 0$
Vacuum	$z = 0$	$\frac{\partial c_i}{\partial z} = 0$
		$v = 0$
		$\frac{\partial T}{\partial z} = 0$
	$z = L$	$\frac{\partial P}{\partial z} = \alpha_{blowdown}(P_{vac} - P)$
Pre-heating/Desorption	$z = 0$	$\frac{\partial c_i}{\partial z} = 0$
		$v = 0$
		$\frac{\partial T}{\partial z} = 0$
	$z = L$	$\frac{\partial P}{\partial z} = \alpha_{blowdown}(P_{vac} - P)$
Cooling	$z = 0$	$\frac{\partial c_i}{\partial z} = 0$
		$v = 0$
		$\frac{\partial T}{\partial z} = 0$
	$z = L$	$v = 0$

Heat capacity and viscosity correlations

In this section the property correlations are made using data from NIST.[64]

The dependence of temperature on molar heat capacities has been fitted to a quadratic equation in the range of 273K to 600K in the form of:

$$C_p = A_{cp}T^2 + B_{cp}T + C_{cp}$$

A_{cp}, B_{cp}, and C_{cp} are as follows:

Table S6 Parameters for heat capacity correlations, along with the R^2 coefficient for each fit

Component	A_{cp}	B_{cp}	C_{cp}	R^2
N_2	0.0000106569	-0.0064057779	30.1318	1.00
CO_2	-0.0000323753	0.0617517420	21.9165	1.00
H_2O	0.00172619108	-1.22971184026	250.9868	0.96
O_2	0.00000908259	0.00100528795	28.3000	1.00

The temperature dependence of viscosity at 1 bar (pressure of adsorption step) has been fitted to a linear equation in the range 273K to 600K in the form of:

$$\mu = D_\mu T + E_\mu$$

The parameters are shown below as:

Table S7 Parameters for viscosity correlations, along with the R^2 coefficient for each fit

Component	D_μ	E_μ	R^2
N_2	3.96929E-8	6.15036E-6	1.00
CO_2	4.41697E-8	1.90440E-6	1.00
H_2O	3.55595E-8	-9.930767E-7	1.00
O_2	4.75391E-8	6.53871E-6	1.00

Lewatit® VP OC 1065 properties

The heat capacity has been experimentally determined as 1.58 kJ kg^{-1} K^{-1} by Sonnleitner et al. in 2018[65], which mentions that this is measured during the conditioning step, which is when the material is heated to 95 °C. This is similar to the value of 1.5 kJ kg^{-1} K^{-1} assumed by Veneman et al. in 2015.[37]

The bead size ranges between 0.315 mm and 1.25 mm, with an effective size of 0.47 mm and 0.57 mm. So the average effective bead diameter is 0.52 mm, with a radius of 0.26 mm.[66]

The bulk density is given by the manufacturer as 630 kg m^{-3} to 710 kg m^{-3}.[66] However, in the laboratory, we observed this to be lower. Given a bed voidage of 0.4, we agree with Veneman et al. that the pellet density is 880 kg m^{-3}.[67]

The pore volume is given to be 0.27 cm^3 g^{-1}.[66] Using the pellet density above, the volume of 1g of pellet is 1.136 cm^3, so the voidage of the pellet $\epsilon_p = 0.238$.

Now using the equation below for total voidage:

$$\epsilon_t = \epsilon_b + \epsilon_p(1 - \epsilon_b)$$

$$\epsilon_t = 0.54$$

Linear driving force constants

Linear driving force constants were estimated by fitting the column model to breakthrough data. A simple schematic of the dynamic breakthrough rig is depicted in Figure S15.

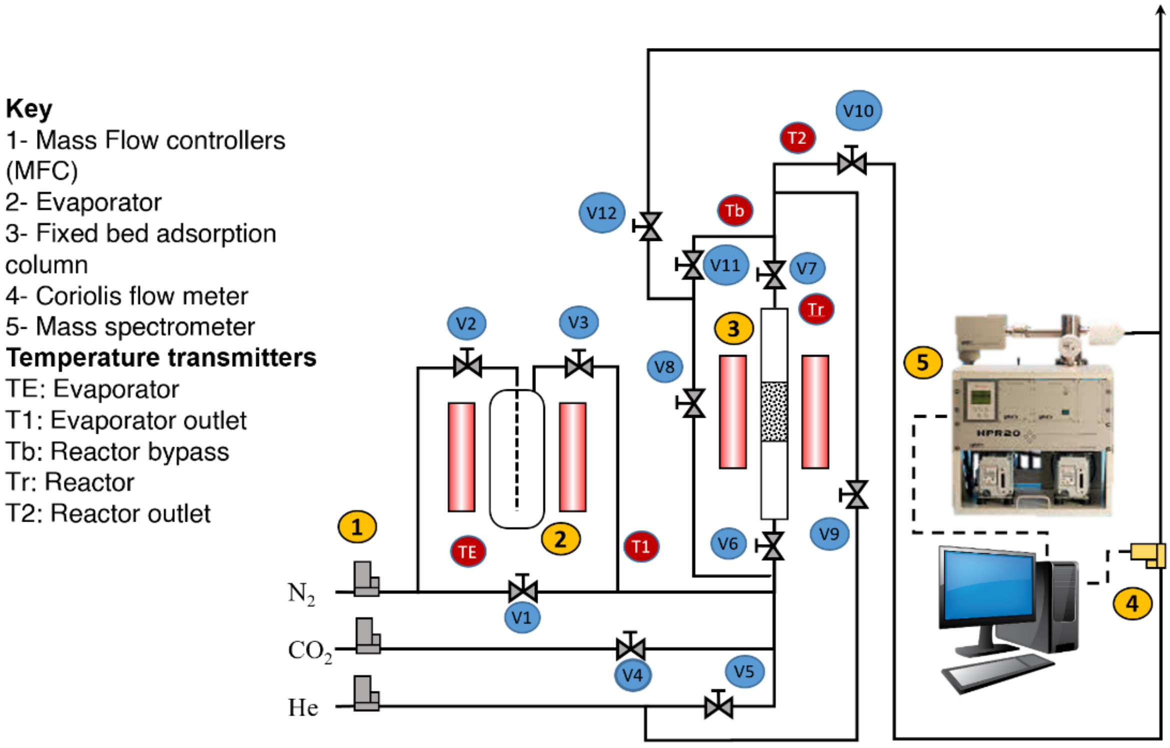

Figure S15 A simple schematic showing the dynamic breakthrough rig

In the following text, numbers in brackets refer to the yellow labels in the figure. The fixed-bed adsorption column (3) is contained in a furnace to ensure isothermal operation. The bed height and mass is measured when the sample is loaded into the column, and it is fixed in place using coarse wool. Mass flow controllers (1) are used to control the flow rate of each component in the feed. The relative humidity is controlled by bubbling the nitrogen stream through the evaporator (2) at a temperature controlled by the heating/cooling jacket around the bubbler. The composition at the outlet of the column is monitored by the mass spectrometer (5), whilst the total flow rate is monitored by the coriolis mass flow meter (4). Before each experiment, around 1 g of Lewatit VP OC 1065® of sample is dried overnight at 95 °C in an oven. Around 200 mg of the dried sample is then used in the experiment and before the adsorption step, the bed is heated to 95 °C under an inert helium flow to ensure proper outgassing. When no more water or carbon dioxide is measured in the mass spectrometer, the reactor is closed, while containing helium as the only gas. The bed is then cooled to the adsorption temperature without any additional adsorption. Finally, adsorption is started once the correct temperature has been reached. Three different adsorption temperatures were investigated, 25, 50, and 70 °C, and at each temperature. 25°C 30% relative humidity was also investigated to extract a mass transfer coefficient for water. The breakthroughs were conducted at atmospheric pressure, and the composition of CO_2 was kept constant at 1%. To do this, the nitrogen flow rate was varied with relative humidity. The total feed flow rate was kept constant at 40.4 ml/min (standard temperature and pressure). The composition of CO_2 used is higher than that of which would be relevant to DAC, but the concentration is still much lower than that used for post-combustion capture and it can be considered very dilute. A lower concentration could not be used due to limitations of the experimental set-up. Each experiment was repeated without any sorbent present to calculate the residence time of the components in the system for the specific conditions. This residence was then used to take into account the residence time of the system when modelling.

The model also can operate isothermally, which describes the column operation used in the dynamic breakthrough rig. The energy balance then becomes:

$$\frac{\partial T}{\partial t} = 0$$

Table S8 show the parameters used in the column model for breakthrough modelling. Due to experimental and time limitations only one humidity and temperature was investigated for H_2O breakthroughs.

Table S8 Parameters used for breakthrough column modelling. Calculations and correlations can be found in this section above.

Parameter	Value	Unit	Source
$\boldsymbol{n_{feed}}$	3.00×10^{-5}	$mol\ s^{-1}$	Measurement
$\boldsymbol{D_m}$	1.30×10^{-5}	$m^2 s^{-1}$	Calculated
$\boldsymbol{C_{p,f}}$	Correlations	$J\ mol^{-1}\ K^{-1}$	[64]
$\boldsymbol{\mu}$	Correlations	$Pa\ s$	[64]
$\boldsymbol{C_{p,s}}$	1580	$J\ kg^{-1}\ K^{-1}$	[65]
$\boldsymbol{R_p}$	0.26	mm	[66]
$\boldsymbol{\rho_p}$	880	$kg\ m^{-3}$	[67]
$\boldsymbol{\epsilon_b}$	0.4	-	Assumption
$\boldsymbol{\epsilon_t}$	0.54	-	Calculated
$\boldsymbol{L}$	Varies slightly across experiments	m	Measurement
$\boldsymbol{d}$	0.0067	m	Measurement
$\boldsymbol{T_{feed}}$	Varied	K	Controlled
$\boldsymbol{RH_{feed}}$	Varied	-	Controlled
$\boldsymbol{x_{CO_2,feed}}$	0.01	-	Controlled
$\boldsymbol{P_{out}}$	1.01325×10^5	Pa	Atmospheric pressure
Energy balance	Isothermal	-	Controlled

Figures S16 and S17 show CO_2 and H_2O breakthroughs respectively. A linear driving force constant of 0.003 s^{-1} was fitted to all three temperatures shown for CO_2 adsorption, whilst a linear driving force constant of 0.0086 s^{-1} was fitted to the breakthrough curve for water adsorption.

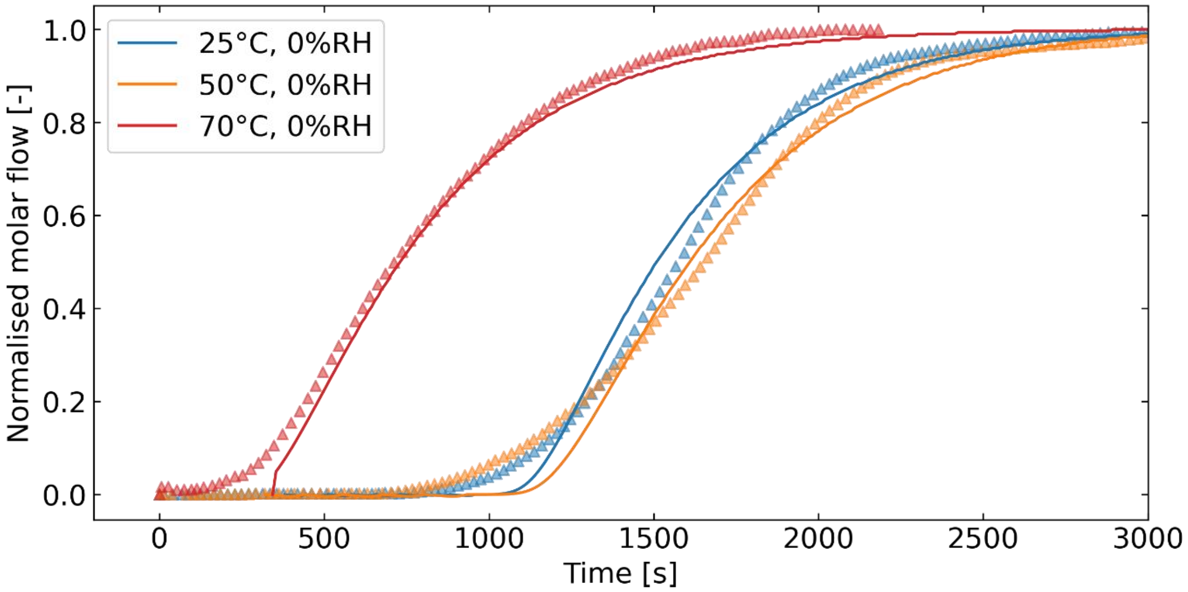

Figure S16 Experimental CO_2 breakthrough curves (triangle markers) alongside modelled values (lines). The offset seen in the 70°C experiment is due to the measured residence time of the system being added to the modelled time values.

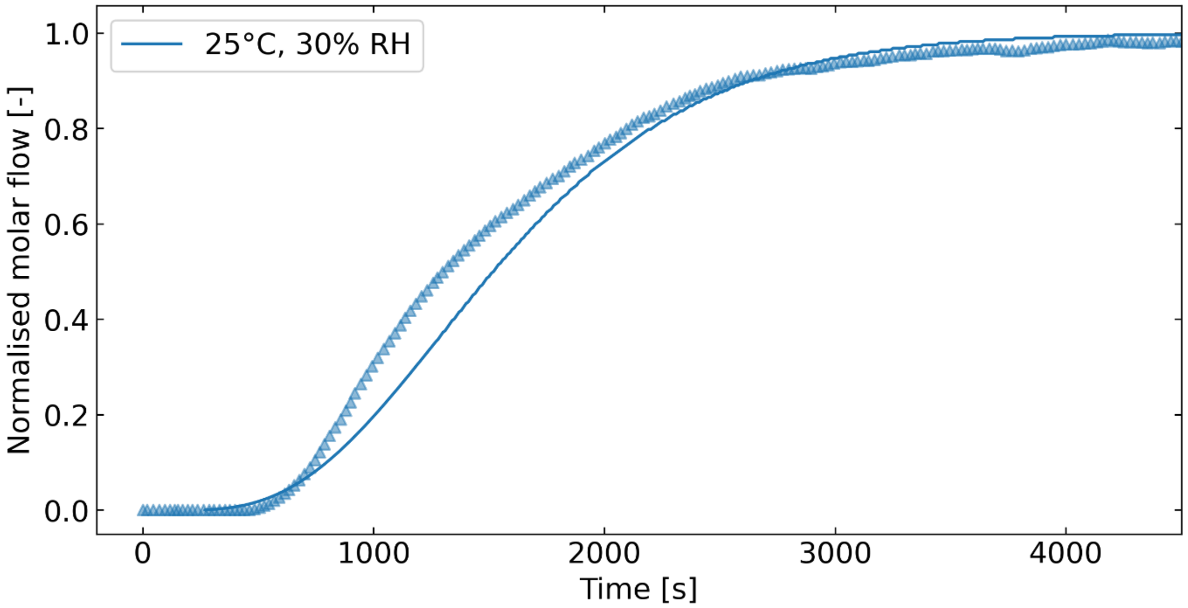

Figure S17 Experimental H_2O breakthrough curve (triangle markers) alongside modelled value (lines).

Model validation

Figure S18 show how the results from the model compare to work by Joss et al.[68] The profiles shown are at the end of the column for a TSA cycle, involving open heating, closed cooling, pressurisation, and adsorption in that order. The slight difference in temperature profiles could be because the work by Joss et al. includes a wall energy balance, whereas this study just considers overall heat transfer from the jacket fluid to the column inside. And then, this temperature difference likely causes a slight variation in the mole fraction profiles, particularly during the heating step. Alternatively, the difference may be due to a slight difference in numerical solution, due to the two pieces of work using different discretisation schemes and ordinary differential equation solvers.

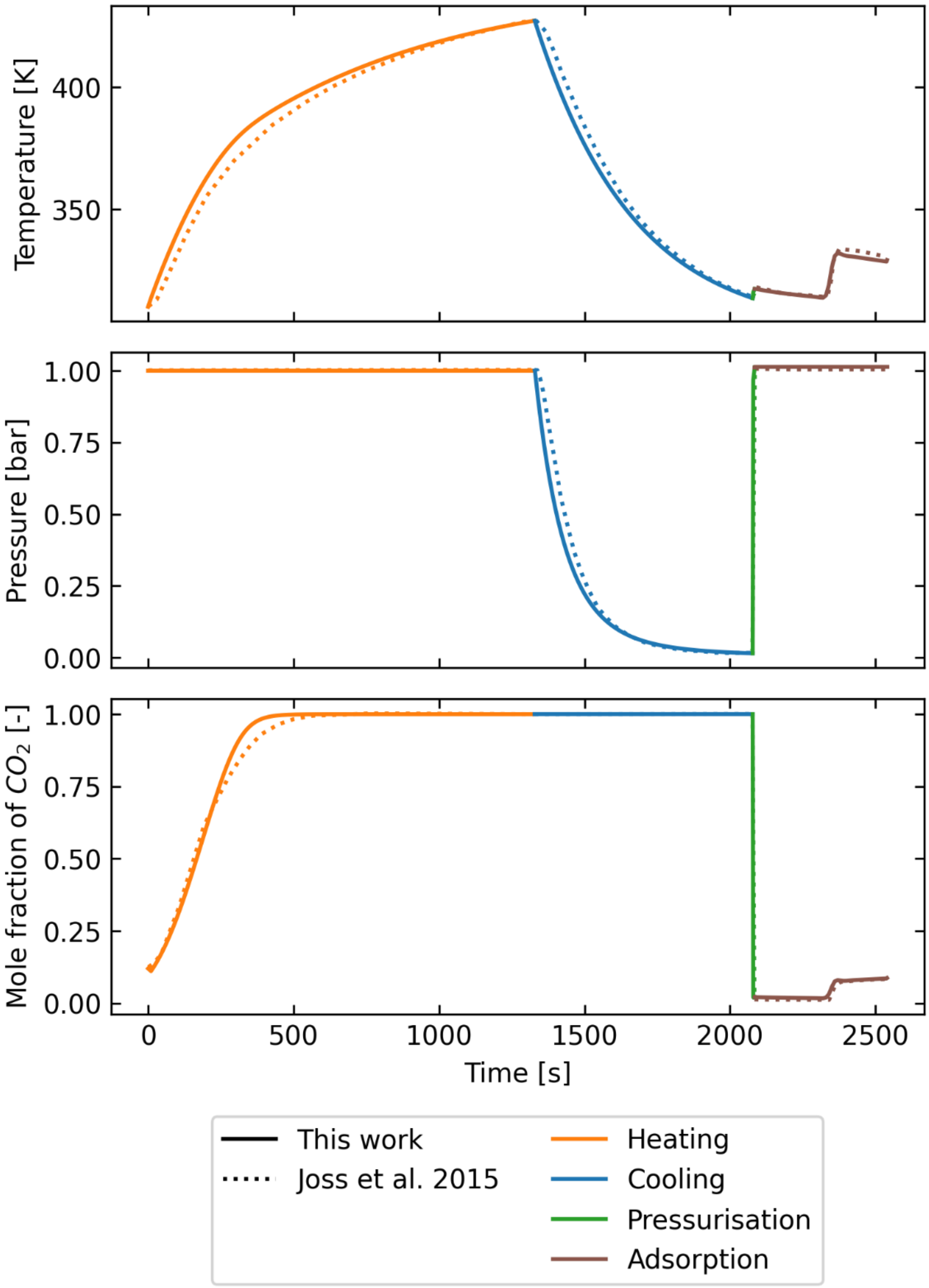

Figure S18 Profiles at the column end for the validation case of the detailed column model. This work is shown by solid lines and work by Joss et al. is shown by the dotted lines. The steps are open heating (orange), closed cooling (blue), pressurisation (green), and adsorption (brown)

Parameters used

Table S9 shows the parameters used for the TVSA DAC modelling case used to compare the effect of each different co-adsorption isotherm model on column profiles. It was assumed the column began saturated under feed conditions. All the isotherm models used are the ones developed and/or fitted in this work. The heat transfer coefficient, h_j, was a value found when validating the model against work by Joss et al. and this is assumed to be a reasonable value for the modelling study considered here. [68]

The heat transfer coefficient mainly affects the heating and cooling times, which would impact the productivity of the process. Hence the productivity values calculated in this work should be taken with caution. For the sake of this study, it is the relative values, rather than the absolute values, that is important.

Table S9 Parameters used for the baseline DAC cycle modelling. Calculations and correlations can be found in this section above.

Parameter	Value	Unit	Source
Fluid properties			
$\boldsymbol{C_{p,f}}$	Correlations	$J\ mol^{-1}\ K^{-1}$	[64]
$\boldsymbol{\mu}$	Correlations	$Pa\ s$	[64]
$\boldsymbol{\gamma_{gas}}$	1.4	$-$	Assumption
Adsorbent and bed properties			
$\boldsymbol{C_{p,s}}$	1580	$J\ kg^{-1}\ K^{-1}$	[65]
$\boldsymbol{R_p}$	0.26	mm	[66]
$\boldsymbol{\rho_p}$	880	$kg\ m^{-3}$	[67]
$\boldsymbol{k_{LDF,CO_2}}$	0.003	s^{-1}	Breakthroughs (see Figure S16)
$\boldsymbol{k_{LDF,H_2O}}$	0.0086	s^{-1}	Breakthroughs (see Figure S17)
$\boldsymbol{\Delta H_{CO_2}}$	$-70{,}000$	$J\ mol^{-1}$	Experimental results.
$\boldsymbol{\Delta H_{H_2O}}$	$-46{,}000$	$J\ mol^{-1}$	Experimental results
$\boldsymbol{\epsilon_b}$	0.4	-	Assumption
$\boldsymbol{\epsilon_t}$	0.54	-	Calculated
Column specifications			
$\boldsymbol{L}$	0.01	m	[29]
$\boldsymbol{d}$	0.1	m	Assumption. Flat bed. [29]
$\boldsymbol{h_j}$	14	$W\ m^{-2}\ K^{-1}$	Reasonable value from model validation
Equipment specifications			
$\boldsymbol{\eta_{vac}}$	0.7	$-$	[69]
$\boldsymbol{\eta_{blower}}$	0.5	$-$	[69]
Feed conditions			
$\boldsymbol{D_m}$	1.30×10^{-5}	$m^2 s^{-1}$	Calculated
$\boldsymbol{v_{feed}}$	7.06×10^{-2}	$m\ s^{-1}$	Calculated. 90% of the minimum fluidisation.
$\boldsymbol{T_{feed}}$	288.15	K	Chosen feed conditions.
$\boldsymbol{RH_{feed}}$	0.55	-	Highest experimental isotherm relative humidity.
$\boldsymbol{x_{CO_2,feed,dry}}$	0.0004	-	Mole fraction of CO_2 in dry air.
$\boldsymbol{P_{out}\ /\ P_{feed}}$	1.01325×10^5	Pa	Atmospheric pressure
Operating conditions			
$\boldsymbol{P_{vac}}$	2×10^4	Pa	Reasonable value.
$\boldsymbol{T_{j,heat}\ /\ T_{j,des}}$	373.15	K	Limited by sorbent stability. [66]
$\boldsymbol{T_{j,ads}\ /\ T_{j,cool}}$	288.15	K	Same as chosen feed conditions.

$\boldsymbol{t_{vac}}$	60	s	-
$\boldsymbol{t_{heat}}$	2400	s	-
$\boldsymbol{t_{des}}$	20,000	s	-
$\boldsymbol{t_{cool}}$	400	s	-
$\boldsymbol{t_{press}}$	60	s	-
$\boldsymbol{t_{ads}}$	8000	s	-

HEURISTIC OPTIMISATION

Distributions of input parameters

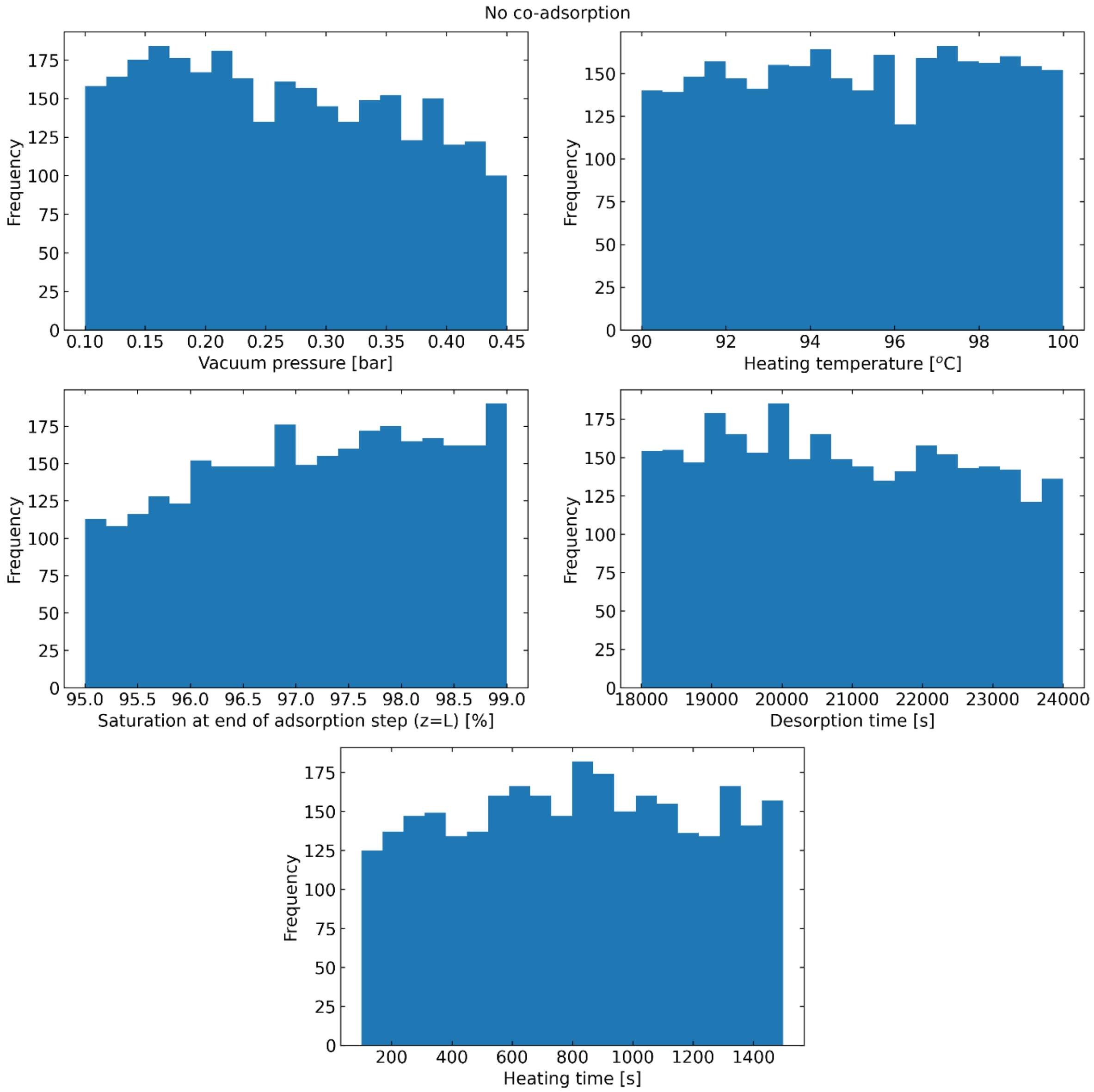

Figure S19 Histogram showing the distribution of factors from the Monte Carlo simulations when using the no co-adsorption isotherm model.

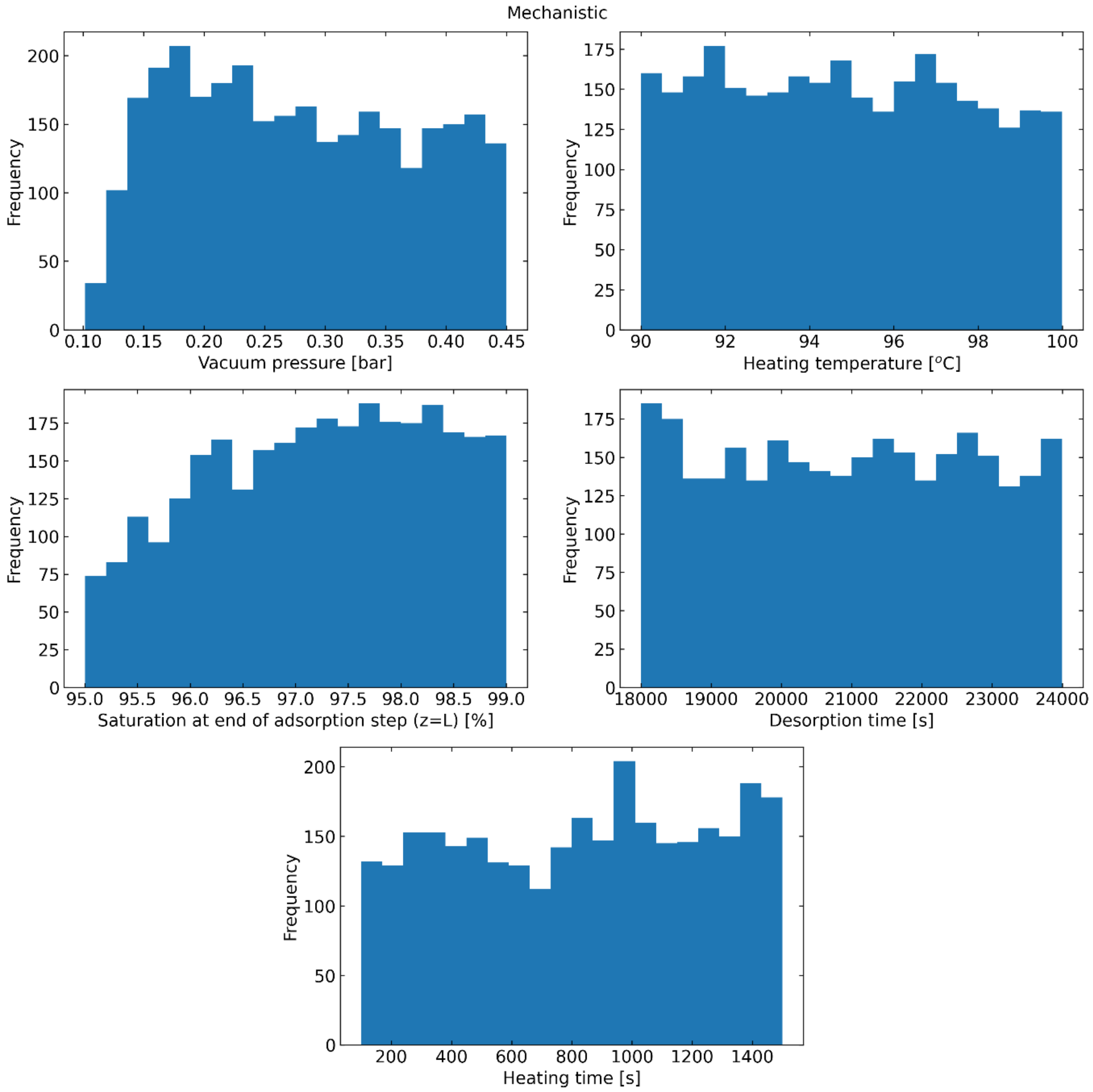

Figure S20 Histogram showing the distribution of factors from the Monte Carlo simulations when using the mechanistic co-adsorption isotherm model.

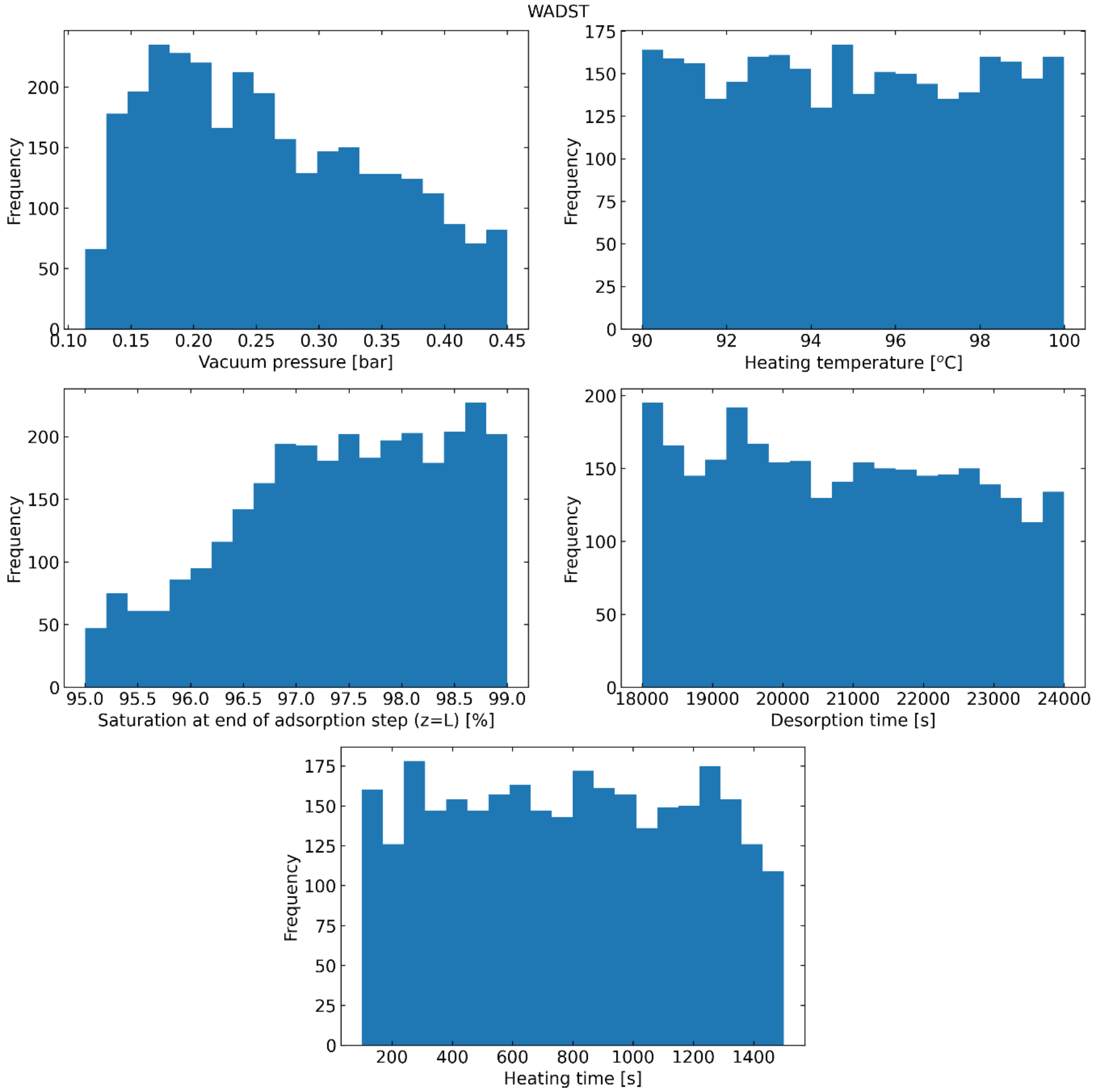

Figure S21 Histogram showing the distribution of factors from the Monte Carlo simulations when using the WADST co-adsorption isotherm model.

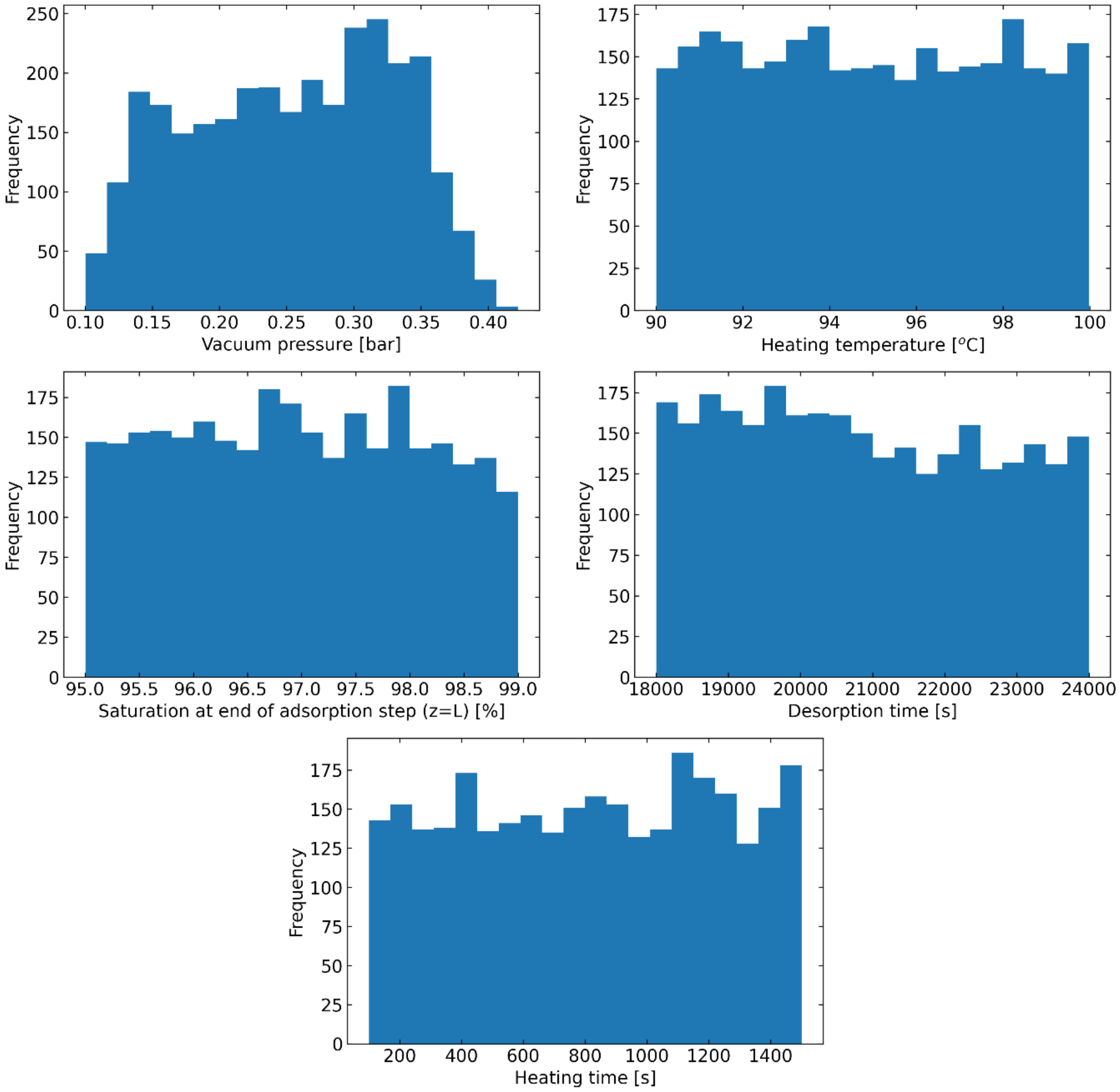

Figure S22 Histogram showing the distribution of factors from the Monte Carlo simulations when using the empirical literature co-adsorption isotherm model.

Additional results

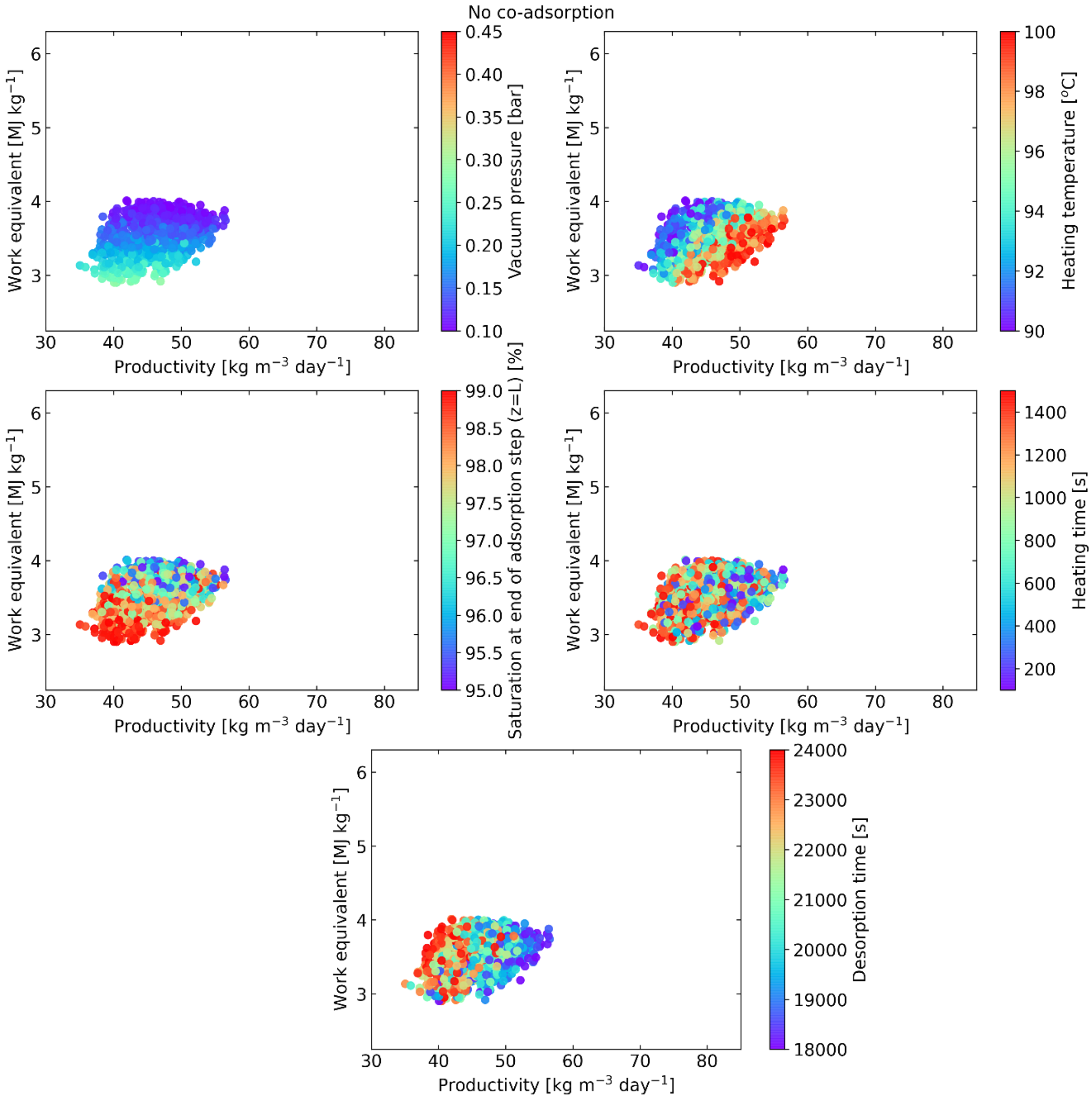

Figure S23 Scatter plots showing work equivalent vs productivity for samples that show a purity of greater than 95% as predicted when applying no co-adsorption isotherm model. Each scatter plot shows the same points coloured by the different operating variables that are being varied according to the range that they are being varied in.

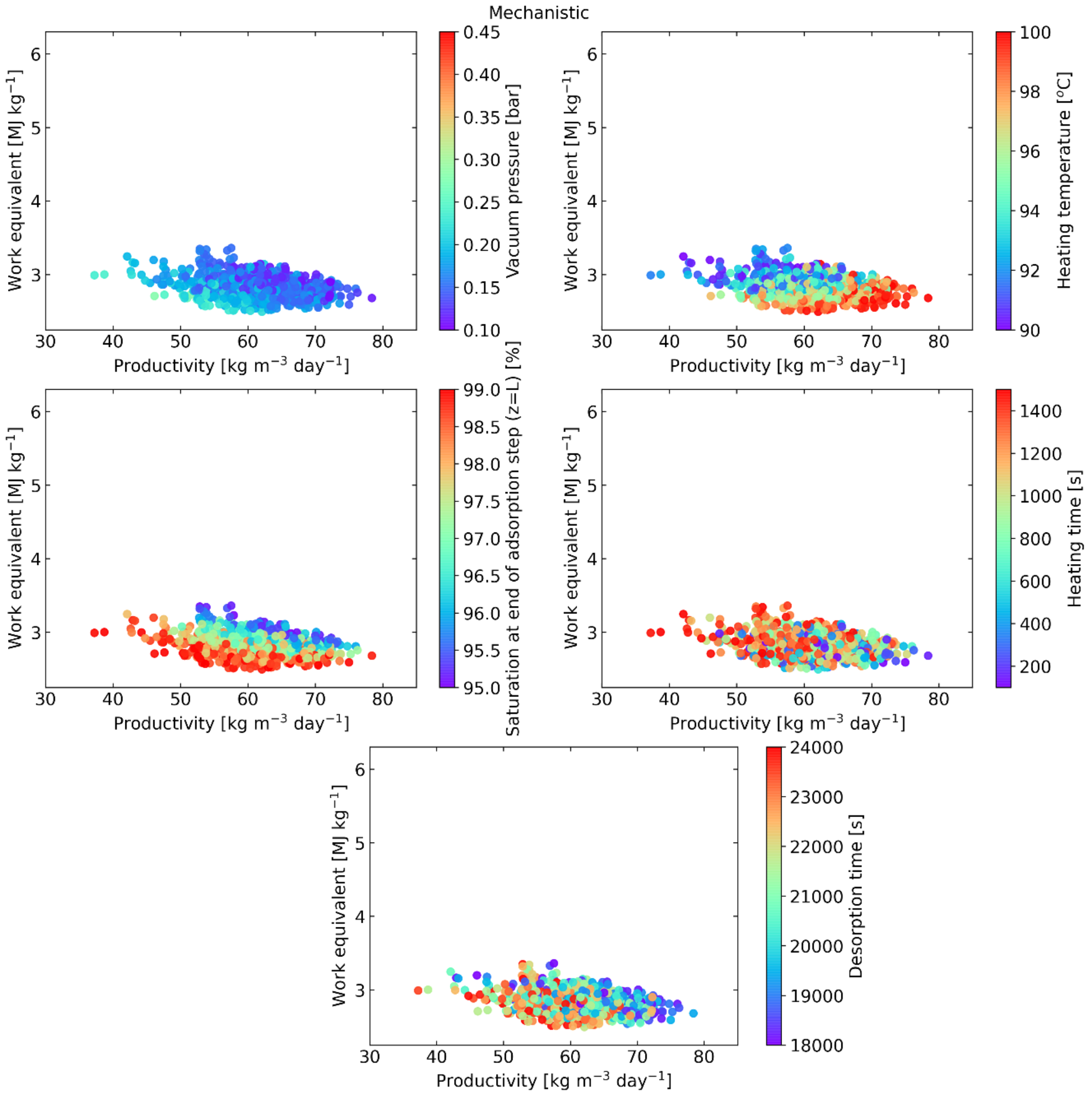

Figure S24 Scatter plots showing work equivalent vs productivity for samples that show a purity of greater than 95% as predicted when applying the mechanistic isotherm model. Each scatter plot shows the same points coloured by the different operating variables that are being varied according to the range that they are being varied in.

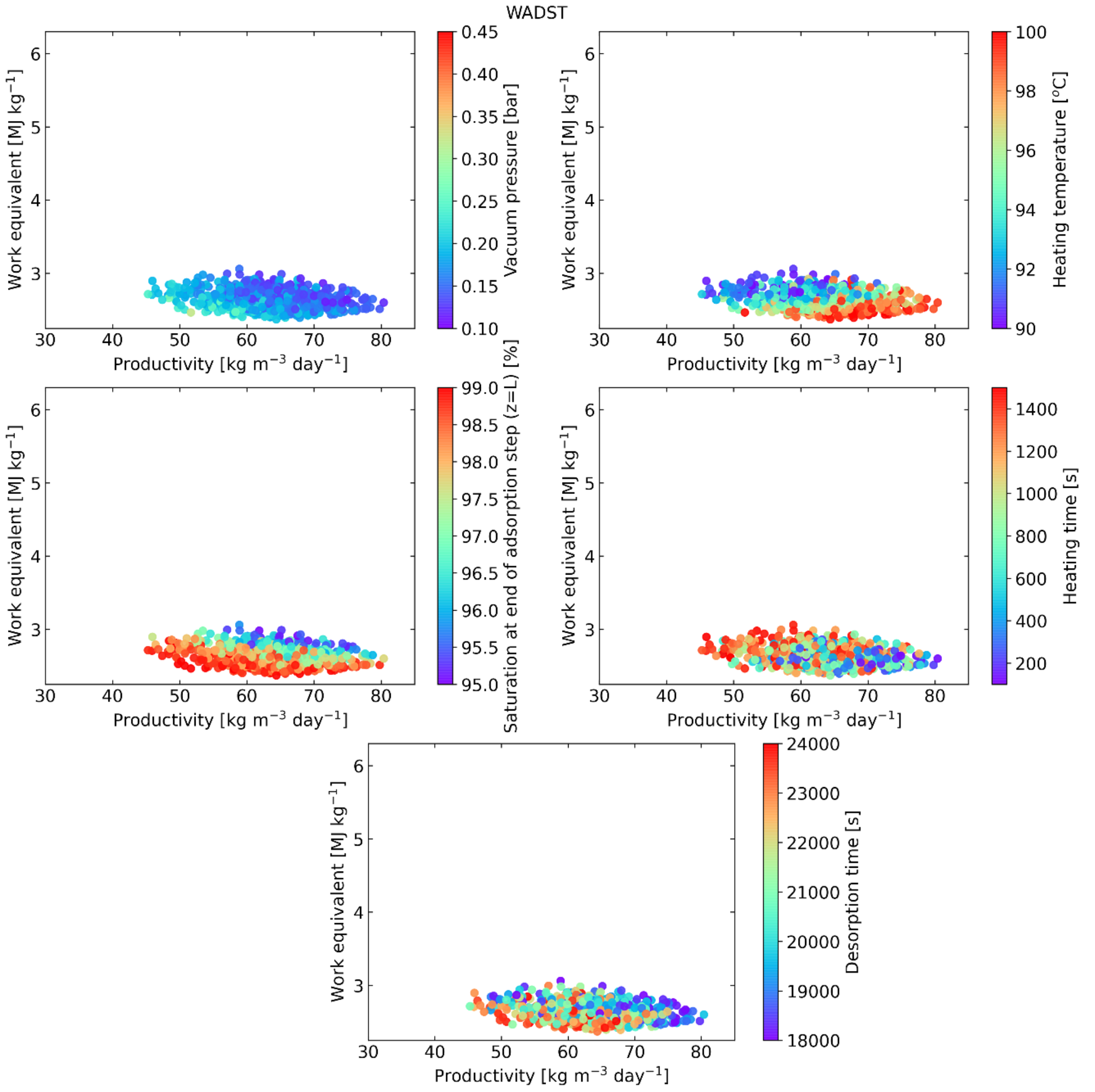

Figure S25 Scatter plots showing work equivalent vs productivity for samples that show a purity of greater than 95% as predicted when applying the WADST co-adsorption isotherm model. Each scatter plot shows the same points coloured by the different operating variables that are being varied according to the range that they are being varied in.

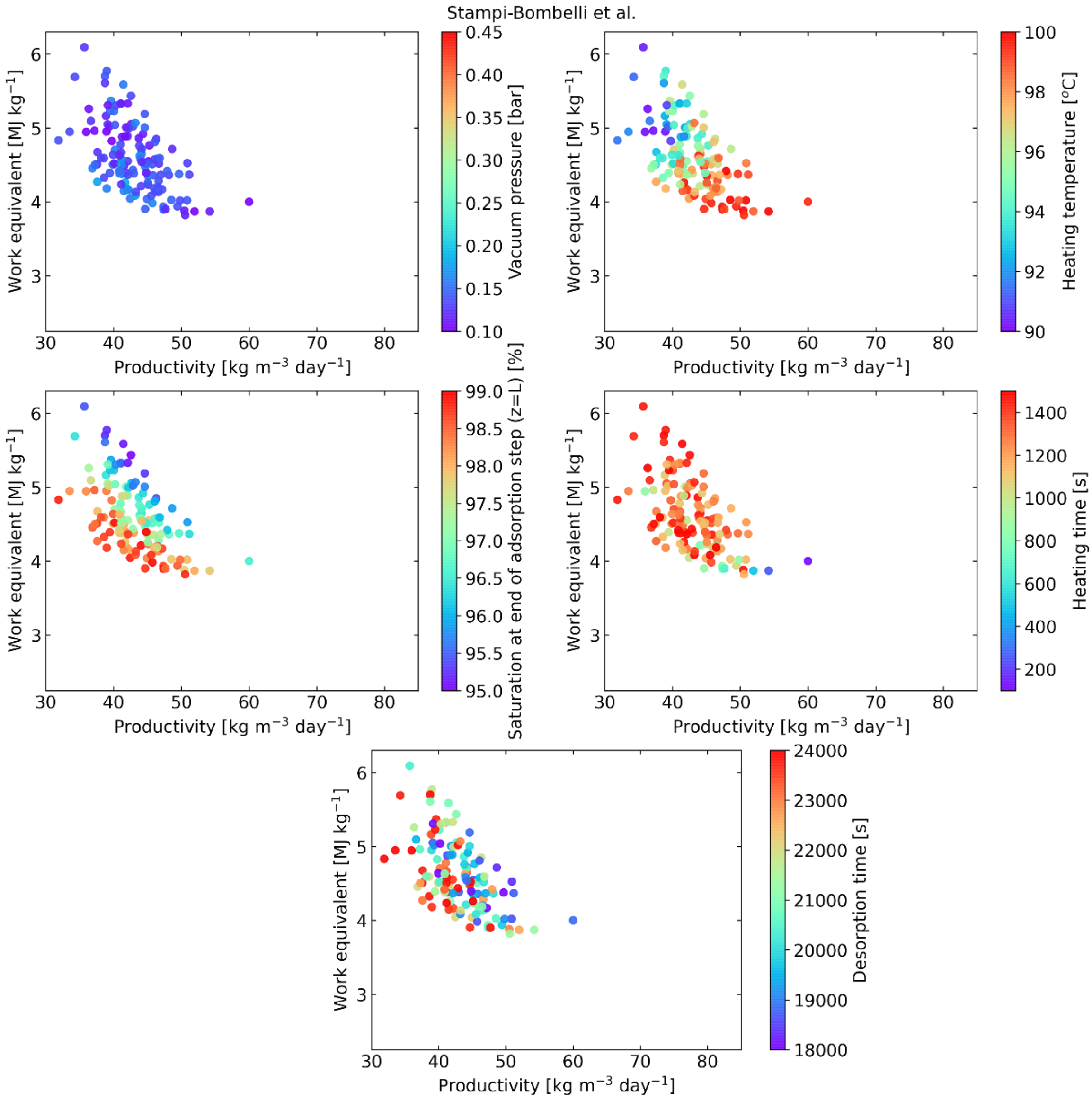

Figure S26 Scatter plots showing work equivalent vs productivity for samples that show a purity of greater than 95% as predicted when applying the empirical literature co-adsorption isotherm model. Each scatter plot shows the same points coloured by the different operating variables that are being varied according to the range that they are being varied in.

Optimal points

Table S10 Operating conditions and performance indicators for predicted minimum work equivalent and maximum productivity by using each co-adsorption isotherm modelling approach.

Isotherm model	**No co-adsorption**		**Mechanistic**		**WADST**		**Stampi-Bombelli et al.**	
Performance indicator optimised	W^{eq}	Pr	W^{eq}	Pr	W^{eq}	Pr	W^{eq}	Pr
Vacuum pressure [bar]	0.28	0.13	0.22	0.11	0.20	0.12	0.12	0.10
Heating temperature [°C]	98.03	99.25	99.92	99.89	99.73	99.73	99.35	99.48
End of column saturation [%]	98.94	95.42	98.86	98.83	98.95	97.71	98.79	96.57
Desorption time [s]	23371	18826	21803	19398	23033	19676	21377	18850
Heating time [s]	877	251	607	162	856	130	1147	124
Purity [%]	95.22	96.06	96.50	98.65	97.45	97.46	99.42	95.72
Working capacity [mol kg^{-1}]	0.61	0.70	0.91	1.05	1.00	1.08	0.71	0.74
Specific heat energy [MJ kg^{-1}]	12.65	12.92	9.93	8.86	9.19	8.78	12.90	13.00
Specific mechanical work [MJ kg^{-1}]	0.78	1.55	0.80	1.17	0.80	1.11	1.63	1.79
Specific work equivalent [MJ kg^{-1}]	2.90	3.74	2.49	2.68	2.37	2.60	3.82	4.00
Productivity [kg m^{-3} day^{-1}]	40.47	56.55	62.09	78.40	64.40	80.40	50.58	60.01

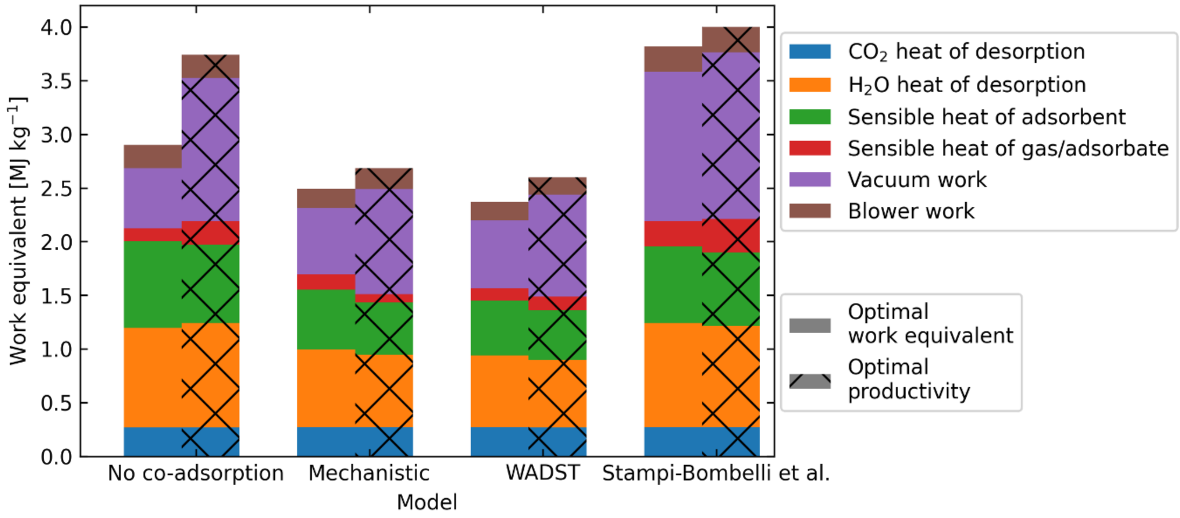

Figure S27 A breakdown of the contributions of the specific work equivalent for 8 different cases. These are the lowest work equivalent and highest productivity cases for each co-adsorption isotherm model. The cases are described in more detail in Table S10.

Working capacity comparison

Table S11 Operating conditions and performance indicators for two points from the mechanistic and WADST model with equivalent working capacities.

Isotherm model	**Mechanistic**	**WADST**
Working capacity [mol kg^{-1}]	1.08	1.08
Vacuum pressure [bar]	0.11	0.12
Heating temperature [°C]	99.60	99.18
End of column saturation [%]	98.12	97.71
Desorption time [s]	22391	19676
Heating time [s]	238	130
Purity [%]	98.53	97.46
Specific heat energy [MJ kg^{-1}]	8.89	8.78
Specific mechanical work [MJ kg^{-1}]	1.20	1.11
Specific work equivalent [MJ kg^{-1}]	2.72	2.60
Productivity [kg m^{-3} day^{-1}]	74.8	83.2

COMPRESSION ELECTRICAL ENERGY CALCULATION

The additional energy to compress CO_2 from atmospheric pressure was found to be 0.44 MJ kg^{-1}. The assumptions for this are:

- All the water is condensed out prior to compression.
- An isentropic efficiency of 0.75.
- A CO_2 purity of 95% with respect to just CO_2 and N_2.
- A maximum compression ratio of 3 in one stage, and the number of stages is minimised given this.
- After each stage, the stream is cooled back down to ambient temperature (15°C).

HEAT TRANSFER COEFFICIENT SENSITIVITY

A sensitivity analysis to investigate the effect of the heat transfer coefficient on the process performance indicators is performed. We took the minimum work equivalent case using the mechanistic isotherm model and varied the heat transfer coefficient by +/- 30%. To make a fair comparison, we also had to vary the cooling, heating, and desorption times to ensure that the same temperature level is reached at the end of each of these steps. The results are shown in Figure S28.

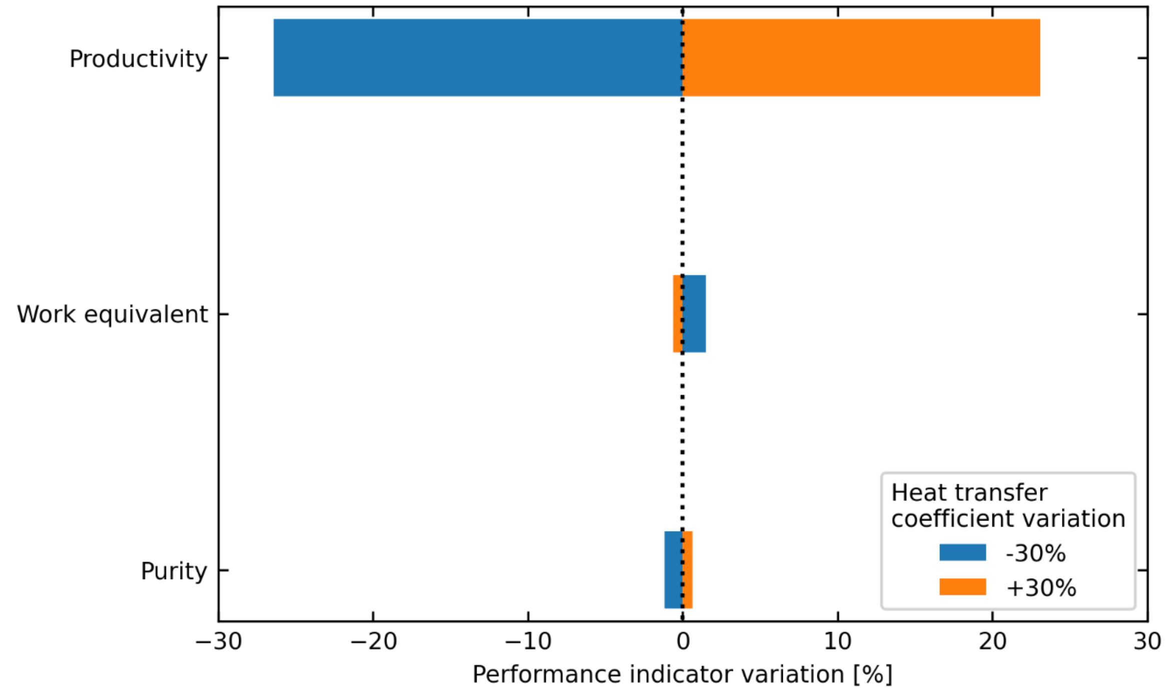

Figure S28 A sensitivity analysis showing the effect of varying the heat transfer coefficient on the performance indicators.

The results in Figure S28 show that the heat transfer coefficient does not significantly impact work equivalent or purity. It does, however, have a large effect on productivity, as expected. Ultimately, since the same temperature levels are reached after each step, the loadings and concentrations reached at the end of each step are very similar. However, the cooling, heating, and desorption step times change. As a result, the total cycle time increases when the heat transfer coefficient is decreased and decreases when the heat transfer coefficient is increased. Hence, the heat transfer coefficient significantly impacts productivity and will be an area for further process optimisation in the future.

REFERENCES

1 E. S. Sanz-Pérez, C. R. Murdock, S. A. Didas and C. W. Jones, *Chem. Rev.*, 2016, **116**, 11840–11876.

2 S. A. Didas, A. R. Kulkarni, D. S. Sholl and C. W. Jones, *ChemSusChem*, 2012, **5**, 2058–2064.

3 S. Satyapal, T. Filburn, J. Trela and J. Strange, *Energy and Fuels*, 2001, **15**, 250–255.

4 Z. Chen, S. Deng, H. Wei, B. Wang, J. Huang and G. Yu, *ACS Appl. Mater. Interfaces*, 2013, **5**, 6937–6945.

5 M. Niu, H. Yang, X. Zhang, Y. Wang and A. Tang, *ACS Appl. Mater. Interfaces*, 2016, **8**, 17312–17320.

6 M. A. Sakwa-Novak and C. W. Jones, *ACS Appl. Mater. Interfaces*, 2014, **6**, 9245–9255.

7 A. Abdollahi-Govar, A. D. Ebner and J. A. Ritter, *Energy and Fuels*, 2015, **29**, 4492–4502.

8 A. R. Sujan, S. H. Pang, G. Zhu, C. W. Jones and R. P. Lively, *ACS Sustain. Chem. Eng.*, 2019, **7**, 5264–5273.

9 A. Heydari-Gorji and A. Sayari, *Chem. Eng. J.*, 2011, **173**, 72–79.

10 W. R. Lee, S. Y. Hwang, D. W. Ryu, K. S. Lim, S. S. Han, D. Moon, J. Choi and C. S. Hong, *Energy Environ. Sci.*, 2014, **7**, 744–751.

11 T. M. McDonald, W. R. Lee, J. A. Mason, B. M. Wiers, C. S. Hong and J. R. Long, *J. Am. Chem. Soc.*, 2012, **134**, 7056–7065.

12 G. Zhang, P. Zhao, L. Hao and Y. Xu, *J. CO2 Util.*, 2018, **24**, 22–33.

13 E. S. Sanz-Pérez, A. Arencibia, G. Calleja and R. Sanz, *Microporous Mesoporous Mater.*, 2018, **260**, 235–244.

14 A. Goeppert, M. Czaun, R. B. May, G. K. S. Prakash, G. A. Olah and S. R. Narayanan, *J. Am. Chem. Soc.*, 2011, **133**, 20164–20167.

15 A. Goeppert, H. Zhang, M. Czaun, R. B. May, G. K. S. Prakash, G. A. Olah and S. R. Narayanan, *ChemSusChem*, 2014, **7**, 1386–1397.

16 S. Choi, J. H. Drese, P. M. Eisenberger and C. W. Jones, *Environ. Sci. Technol.*, 2011, **45**, 2420–2427.

17 Y. Belmabkhout, R. Serna-guerrero and A. Sayari, *Adsorpt. J. Int. Adsorpt. Soc.*, 2010, **49**, 359–365.

18 M. A. Sakwa-Novak, S. Tan and C. W. Jones, *ACS Appl. Mater. Interfaces*, 2015, **7**, 24748–24759.

19 W. Chaikittisilp, J. D. Lunn, D. F. Shantz and C. W. Jones, *Chem. - A Eur. J.*, 2011, **17**, 10556–10561.

20 A. Kumar, D. G. Madden, M. Lusi, K. J. Chen, E. A. Daniels, T. Curtin, J. J. Perry and M. J. Zaworotko, *Angew. Chemie - Int. Ed.*, 2015, **54**, 14372–14377.

21 L. A. Darunte, T. Sen, C. Bhawanani, K. S. Walton, D. S. Sholl, M. J. Realff and C. W. Jones, *Ind. Eng. Chem. Res.*, 2019, **58**, 366–377.

22 W. Chaikittisilp, H. J. Kim and C. W. Jones, *Energy and Fuels*, 2011, **25**, 5528–5537.

23 H. He, M. Zhong, D. Konkolewicz, K. Yacatto, T. Rappold, G. Sugar, N. E. David and K. Matyjaszewski, *J. Mater. Chem. A*, 2013, **1**, 6810–6821.

24 J. A. Wurzbacher, C. Gebald, N. Piatkowski and A. Steinfeld, *Environ. Sci. Technol.*, 2012, **46**, 9191–9198.

25 D. W. F. Brilman and R. Veneman, *Energy Procedia*, 2013, **37**, 6070–6078.

26 C. Gebald, J. A. Wurzbacher, P. Tingaut and A. Steinfeld, *Environ. Sci. Technol.*, 2013, **47**, 10063–10070.

27 C. Gebald, J. A. Wurzbacher, A. Borgschulte, T. Zimmermann and A. Steinfeld, *Environ. Sci. Technol.*, 2014, **48**, 2497–2504.

28 J. A. Wurzbacher, C. Gebald, S. Brunner and A. Steinfeld, *Chem. Eng. J.*, 2016, **283**, 1329–1338.

29 V. Stampi-Bombelli, M. van der Spek and M. Mazzotti, *Adsorption*, 2020, **26**, 1183–1197.

30 S. Choi, T. Watanabe, T. H. Bae, D. S. Sholl and C. W. Jones, *J. Phys. Chem. Lett.*, 2012, **3**, 1136–1141.

31 R. Vaidhyanathan, S. S. Iremonger, K. W. Dawson and G. K. H. Shimizu, *Chem. Commun.*, 2009, **35**, 5230–5232.

32 L. A. Darunte, A. D. Oetomo, K. S. Walton, D. S. Sholl and C. W. Jones, *ACS Sustain. Chem. Eng.*, 2016, **4**, 5761–5768.

33 A. Sinha, L. A. Darunte, C. W. Jones, M. J. Realff and Y. Kawajiri, *Ind. Eng. Chem. Res.*, 2017, **56**, 750–764.

34 H. Li, K. Wang, D. Feng, Y. P. Chen, W. Verdegaal and H. C. Zhou, *ChemSusChem*, 2016, **9**, 2832–2840.

35 L. He, M. Fan, B. Dutcher, S. Cui, X. dong Shen, Y. Kong, A. G. Russell and P. McCurdy, *Chem. Eng. J.*, 2012, **189–190**, 13–23.

36 R. Veneman, W. Zhao, Z. Li, N. Cai and D. W. F. Brilman, *Energy Procedia*, 2014, **63**, 2336–2345.

37 R. Veneman, N. Frigka, W. Zhao, Z. Li, S. Kersten and W. Brilman, *Int. J. Greenh. Gas Control*, 2015, **41**, 268–275.

38 M. J. Bos, T. Kreuger, S. R. A. Kersten and D. W. F. Brilman, *Chem. Eng. J.*, 2019, **377**, 120374.

39 M. J. Bos, S. Pietersen and D. W. F. Brilman, *Chem. Eng. Sci. X*, 2019, **2**, 100020.

40 W. Lu, J. P. Sculley, D. Yuan, R. Krishna and H. C. Zhou, *J. Phys. Chem. C*, 2013, **117**, 4057–4061.

41 T. Wang, K. S. Lackner and A. Wright, *Environ. Sci. Technol.*, 2011, **45**, 6670–6675.

42 T. Wang, K. S. Lackner and A. B. Wright, *Phys. Chem. Chem. Phys.*, 2013, **15**, 504–514.

43 X. Shi, Q. Li, T. Wang and K. S. Lackner, *PLoS One*, 2017, **12**, e0179828.

44 H. He, W. Li, M. Lamson, M. Zhong, D. Konkolewicz, C. M. Hui, K. Yaccato, T. Rappold, G. Sugar, N. E. David, K. Damodaran, S. Natesakhawat, H. Nulwala and K. Matyjaszewski, *Polymer (Guildf).*, 2014, **55**, 385–394.

45 H. He, W. Li, M. Zhong, D. Konkolewicz, D. Wu, K. Yaccato, T. Rappold, G. Sugar, N. E. David and K. Matyjaszewski, *Energy Environ. Sci.*, 2013, **6**, 488–493.

46 S. Choi, M. L. Gray and C. W. Jones, *ChemSusChem*, 2011, **4**, 628–635.

47 W. Chaikittisilp, R. Khunsupat, T. T. Chen and C. W. Jones, *Ind. Eng. Chem. Res.*, 2011, **50**, 14203–14210.

48 Y. Kuwahara, D. Y. Kang, J. R. Copeland, P. Bollini, C. Sievers, T. Kamegawa, H. Yamashita and C. W. Jones, *Chem. - A Eur. J.*, 2012, **18**, 16649–16664.

49 J. A. Wurzbacher, C. Gebald and A. Steinfeld, *Energy Environ. Sci.*, 2011, **4**, 3584–3592.

50 N. R. Stuckert and R. T. Yang, *Environ. Sci. Technol.*, 2011, **45**, 10257–10264.

51 S. J. Datta, C. Khumnoon, Z. H. Lee, W. K. Moon, S. Docao, T. H. Nguyen, I. C. Hwang, D. Moon, P. Oleynikov, O. Terasaki and K. B. Yoon, *Sci. Reports*, 2015, **350**, 302–306.

52 O. Shekhah, Y. Belmabkhout, Z. Chen, V. Guillerm, A. Cairns, K. Adil and M. Eddaoudi, *Nat. Commun.*, 2014, **5**, 4228.

53 D. G. Madden, H. S. Scott, A. Kumar, K.-J. Chen, R. Sanii, A. Bajpai, M. Lusi, T. Curtin, J. J. Perry and M. J. Zaworotko, *Philos. Trans. R. Soc. A Math. Phys. Eng. Sci.*, 2017, **375**, 20160025.

54 P. M. Bhatt, Y. Belmabkhout, A. Cadiau, K. Adil, O. Shekhah, A. Shkurenko, L. J. Barbour and M. Eddaoudi, *J. Am. Chem. Soc.*, 2016, **138**, 9301–9307.

55 G. Santori, C. Charalambous, M. C. Ferrari and S. Brandani, *Energy*, 2018, **162**, 1158–1168.

56 J. P. Young, V. Martis, S. Garcia and M. van der Spek, *11th Trondheim Conf. CO2 Capture, Transp. Storage.*, in press.

57 Micromeritics', 2021.

58 S. Ergun, *Chem. Eng. Prog.*, 1952, **48**, 89–94.

59 W. R. Alesi and J. R. Kitchin, *Ind. Eng. Chem. Res.*, 2012, **51**, 6907–6915.

60 E. Glueckauf and J. I. Coates, *J. Chem. Soc.*, 1947, 1315–1321.

61 A. L. Buck, *J. Appl. Meteorol.*, 1981, **20**, 1527–1532.

62 D. M. Ruthven, *Principles of Adsorption & Adsorption Processes*, John Wiley & Sons, 1984.

63 A. Streb, M. Hefti, M. Gazzani and M. Mazzotti, *Ind. Eng. Chem. Res.*, 2019, **58**, 17489–17506.

64 P. J. Linstrom and W. G. Mallard, *J. Chem. Eng. Data*, 2001, **46**, 1059–1063.

65 E. Sonnleitner, G. Schöny and H. Hofbauer, *Biomass Convers. Biorefinery*, 2018, **8**, 379–395.

66 Lanxess, 2021.

67 R. Veneman, T. Hilbers, D. W. F. Brilman and S. R. A. Kersten, *Chem. Eng. J.*, 2016, **289**, 191–202.

68 L. Joss, M. Gazzani, M. Hefti, D. Marx and M. Mazzotti, *Ind. Eng. Chem. Res.*, 2015, **54**, 3027–

3038.

69 S. Krishnamurthy, V. R. Rao, S. Guntuka, P. Sharratt, R. Haghpanah, A. Rajendran, M. Amanullah, I. A. Karimi and S. Farooq, *AIChE J.*, 2014, **60**, 1830–1842.